The Renner Effect in the X̃ ²A″ and Ã ²A′ Electronic States of HSO/HOS

Roman I. Ovsyannikov,[†,§] Tsuneo Hirano,[‡] and Per Jensen*,[†]

[†]FB C − Physikalische und Theoretische Chemie, Bergische Universität, D-42097 Wuppertal, Germany

[‡]Department of Chemistry, Faculty of Science, Ochanomizu University, 2-1-1 Otsuka, Bunkyo-ku, Tokyo 112-8610, Japan

S *Supporting Information*

ABSTRACT: We report a theoretical investigation of the X̃ ²A″ and Ã ²A′ electronic states of HSO/HOS. Three-dimensional potential energy surfaces for the X̃ ²A″ and Ã ²A′ electronic states of HSO/HOS have been calculated ab initio by the core-valence MR-SDCI+Q/[aug-cc-pCVQZ(S,O),aug-cc-pVQZ(H)] method, and near-global potential energy surfaces have been constructed. These surfaces have been used, in conjunction with our computer program DR, for calculating HSO/HOS rovibronic energies in the electronic states X̃ ²A″ and Ã ²A′. Both electronic states have nonlinear equilibrium geometries and they correlate with ²Π states at the H−S−O and H−O−S linear configurations so that they exhibit the double Renner effect. The present DR calculation of the rovibronic energies for the X̃ ²A″ and Ã ²A′ electronic states of HSO/HOS is complicated by the Renner-interaction breakdown of the Born−Oppenheimer approximation and by HSO/HOS isomerization. Calculated energies are reported together with analyses of the rovibronic wave functions for selected states. These analyses explore the interplay between the effects of, on one hand, Renner interaction and, on the other hand, isomerization tunneling in the rovibronic dynamics of HSO/HOS.
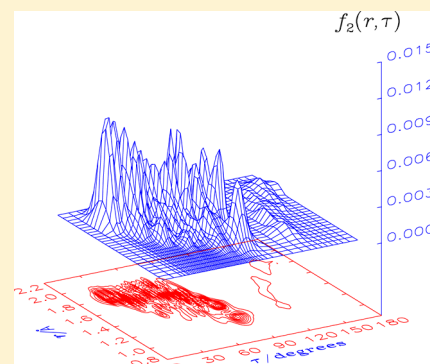
■ INTRODUCTION

In recent years, theoretical simulations of rotation–vibration spectra for molecules of atmospheric and/or astrochemical interest have become increasingly important in studies of the terrestrial atmosphere, "astrophysical" atmospheres, and interstellar space (see, for example, Tennyson[1]). Thus far, such simulations are almost exclusively made in the framework of the Born–Oppenheimer approximation.[2] That is, the theoretical calculations are carried out effectively for one electronic state (generally the ground state) only, this one electronic state having one potential energy surface. For high-precision simulations to be obtained, the influence on the (ground state) rovibronic states considered from rovibronic states associated with other (excited) electronic states cannot be ignored,[1] but as long as the (ground) electronic state considered is energetically well separated from all other electronic states, this influence can be described in terms of perturbation-theory corrections so that in practice, the simulations involve one potential energy surface only. It is well-known, however, that some molecules have interactions between energetically close-lying electronic states that are too strong to be treated as perturbations. To describe such interactions, a variational approach is required in which a truncated matrix representation of the total rovibronic Hamiltonian is constructed and diagonalized numerically. For example, the potential energy surface for the electronic ground state X̃ ²A₁ of the atmospherically relevant NO₂ molecule[3−5] suffers an avoided crossing with that of the low-lying Ã ²B₂ state[4] when the two NO bond lengths are unequal. In addition,

the X̃-state potential energy surface is Renner-degenerate with that of the B̃ ²B₁ state[3] (that is, the two potential energy surfaces are degenerate at linear molecular geometries[6−8]). The astrochemically relevant CCH radical[9] has analogous, strong interactions.

Theoretical calculations of molecular rovibronic energies that explicitly take into account multiple potential energy surfaces can be said to describe the breakdown of the Born–Oppenheimer approximation. Such studies are still at a relatively early stage. However, as the experimental investigation of the Earth's atmosphere, the "astrophysical" atmospheres, and interstellar space progresses, presumably the demands made on the accuracy of theoretical spectral simulations of the molecules involved will increase, and so we expect that in the future, it will become necessary to implement "Born-Oppenheimer breakdown" variationally in the spectral simulation programs. In preparation for this situation, we have studied the so-called Renner (or Renner−Teller) effect for triatomic molecules.[6−8] The Renner effect occurs when two potential energy surfaces of a chain molecule are degenerate at linear molecular geometries (that is, when they generate a doubly degenerate irreducible representation Π, Δ, Φ, ... of the appropriate molecular point group $C_{\infty v}$ or $D_{\infty h}$ at linearity). As

the molecule bends, the two potential energy surfaces split apart and the associated rovibronic basis states are coupled by terms in the kinetic energy operator.[7,10] Initially, we developed the computer program RENNER[11−13] for calculating the rovibronic energies of a triatomic molecule in Renner-degenerate electronic states. RENNER results for the NH_2 radical, whose electronic ground state is Renner-degenerate with the first excited state,[10] have been used for determining the spin temperatures of ammonia in comets (see Kawakita et al.[14] and references therein). However, the culmination of our work on the Renner effect is the development of the computer program[15−19] DR (Double Renner) for obtaining the rovibronic energies and wave functions for triatomic molecules in double-Renner-degenerate electronic states (see below). The DR theory makes use of an exact kinetic energy operator of the type described by Tennyson.[20]

In the present work, the DR program is applied to HSO and HOS, which we consider here as one molecule HSO/HOS. In each of the $\tilde{X}$ $^2A''$ and $\tilde{A}$ $^2A'$ electronic states, HSO/HOS has two strongly bent equilibrium structures with the proton bound to the S or O nucleus, respectively, and separated by a potential energy barrier. In highly excited bending states there is tunneling between the two minima and, in addition, the $\tilde{X}$ $^2A''$ and $\tilde{A}$ $^2A'$ states are degenerate at both the H−S−O and H−O−S linear configurations (where, at each of the linear geometries, the $\tilde{X}$ $^2A''$ and $\tilde{A}$ $^2A'$ states correlate with a state of $^2\Pi$ symmetry in $C_{\infty v}$). Each of the two double degeneracies gives rise to Renner interactions between the $\tilde{X}$ $^2A''$ and $\tilde{A}$ $^2A'$ states; we say that these states are double-Renner-degenerate and the resultant effect is called the double-Renner effect.

As explained above, the HSO/HOS molecule affords an example of the double-Renner effect. This radical is responsible for H_2S oxidation processes in the atmosphere that produce atmospheric H_2SO_4. It is believed that the HS radical is oxidized in the following reactions:[21−23] HS + O_3 → HSO + O_2, HS + NO_2 → HSO + NO. However, the HSO radical is also reduced by O_3: HSO + O_3 → HS + $2O_2$, and so the HSO radical is involved in the ozone depletion cycle.[24,25] This fact has stimulated a number of theoretical[24−30] and experimen-tal[31−39] studies of the HSO-radical spectroscopy. Xantheas and Dunning[26] and Esseffar et al.[27] have reported ab initio estimations of the heat of formation for HSO and of the HSO-HOS isomerization energy. Similar results have been presented by Wang and Howard,[24] Wilson and Dunning,[28] and Wang and Wilson[29] together with predicted vibrational wavenumbers for HSO and HOS. Li et al.[30] have predicted the vertical and adiabatic ionization energies associated with four electronic states of the HSO radical. An observation of the HSO $\tilde{A}$ $^2A'−\tilde{X}$ $^2A''$ band system by chemiluminescence spectroscopy has been reported by Schurath et al.;[31] these authors could assign vibronic bands with prominent ν_3 progressions of HSO for the $\tilde{A}$ state up to $v'_3 = 7$. High resolution studies of the $\tilde{A}$ state[32,33] were made by rotationally resolved laser induced fluorescence (LIF) spectra for the vibronic bands $\tilde{A}(00v'_3)−\tilde{X}(000)$ with $v'_3 = 3$ and 4. Pure rotational spectra for the ground electronic state of the HSO and DSO radicals were observed[37] by millimeter-wave spectroscopy, and accurate molecular constants including the hyperfine coupling constants were determined from the observed data. The ν_3 band in the $\tilde{X}$ state was observed by laser magnetic spectroscopy in the 10 μm region by Sears and McKellar[38] who determined a set of rotational constants from the experimental data. Sears and McKellar[38] further searched

for the ν_2 band below 1100 cm^{-1}, but without success. Yoshikawa et al.[39] later determined the ν_2 band center at 1080.4 cm^{-1} (with the theoretical prediction of the present work being 1087.79 cm^{-1}) using an LIF spectrometer and a pulsed discharge nozzle, and so the reason for the lack of success of Sears and McKellar[38] was probably the low intensity of the band. In addition to measuring the ν_2 band center of HSO, Yoshikawa et al.[39] observed vibronic bands of the $\tilde{A}(00v'_3) − \tilde{X}(000)$ system for $v'_3 = 0−8$ together with the $\tilde{A}(013) − \tilde{X}(001)$ band of HSO. From the observed data, they determined the rotational constants and the spin-rotation interaction constants for the excited electronic state.

We have calculated three-dimensional potential energy surfaces for the $\tilde{X}$ $^2A''$ and $\tilde{A}$ $^2A'$ electronic states of HSO/ HOS ab initio at the core-valence MR-SDCI+Q/[aug-cc-pCVQZ(S,O),aug-cc-pVQZ(H)] level of theory (see the following section for details). From the results of the ab initio calculations, near-global potential energy surfaces for the $\tilde{X}$ $^2A''$ and $\tilde{A}$ $^2A'$ electronic states have been constructed. These surfaces have been used, in conjunction with the computer program DR,[15−17] for calculating HSO/HOS rovibronic energies in the double-Renner-degenerate electronic states. The rovibronic wave functions for selected states have been analyzed.

■ AB INITIO CALCULATIONS

The electronic structure calculations of the present work were made with the ab initio molecular orbital method core-valence MR-SDCI+Q/[aug-cc-pCVQZ(S,O),aug-cc-pVQZ(H)]. Here, MR-SDCI+Q denotes the multireference single and double excitation configuration interaction calculation with Davidson's correction[40] Q to recover the dynamical electron correlation due to quadruple excitations and to obtain partly the size-extensivity. The two lowest electronic states of HSO/HOS are double-Renner-degenerate. Consequently, the two potential energy surfaces of the A′ and A″ states are electronically intercorrelated and it is necessary to use the multireference calculation method. It is well-known in the organic chemistry community that in a molecule, a sulfur atom shows strong pπ−dπ interaction in bonding and reactivity even though it has no d-valence electron. Therefore, we must use a basis set containing "tight d functions", i.e., d-polarization functions with their maximum amplitudes in the region where the sulfur 3p orbitals have their maximum amplitudes. The aug-cc-pCVQZ basis set for sulfur satisfies this requirement. Moreover, core-valence correlation is required to obtain spectroscopic accuracy, and hence we have employed augmented, core-valence quadruple-ζ (CVQZ) basis sets for S[41,42] and O.[43] For H, we have employed the corresponding basis set aug-cc-pVQZ.[43] In summary, the total basis set used in the present work is denoted as [aug-cc-pCVQZ(S,O),aug-cc-pVQZ(H)].

The three-dimensional potential energy surfaces were calculated under C_s symmetry constraint. To ensure that the potential energy functions of the $\tilde{X}$ $^2A''$ and $\tilde{A}$ $^2A'$ states become degenerate at linear geometries of HSO/HOS, and that the $\tilde{X}$ $^2A''$ and $\tilde{A}$ $^2A'$ wave functions at a given point on both surfaces be intercorrelated with each other under the Renner effect, we must carefully treat the symmetries of basis functions and wave functions. Toward this end, it is necessary that the complete active space self-consistent field (CASSCF) calculation be carried out by averaging the two Renner components A′ and A″, i.e., by two-state averaged CASSCF.

To obtain spectroscopic accuracy, we carried out two-state averaged, core-valence CASSCF (13 electrons distributed over 9 orbitals) followed by core-valence MR-SDCI+Q calculations as follows. On the basis of the CASSCF orbitals in this manner, MR-SDCI+Q calculations with full-valence active space (13 electrons distributed over 9 orbitals) have been carried out. To ensure that intercorrelated wave functions were obtained, these calculations included A′ configuration space for the A″ state and A″ configuration space for the A′ state. Here, the core-valence dynamical electron correlation was recovered by the single and double excitations from the doubly occupied subcore orbitals (S 2s and 2p and O 1s orbitals) in each configuration state function (CSF) generated from the active space. Hence, the MR-SDCI method employed here will be denoted as "core-valence MR-SDCI+Q" level of calculation.

We have carried out the actual ab initio calculations as follows, thus satisfying all symmetry requirements. The nuclear geometries and the vibrational motion of HSO/HOS are described by Jacobi coordinates (r, R, τ), which are defined, together with the chosen, right-handed molecule-fixed axis system xyz, in Figure 1. Initially we calculated, in terms of the
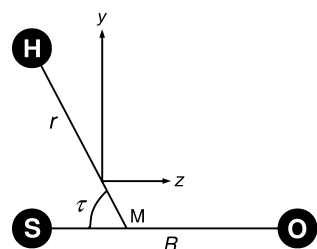

Figure 1. Jacobi coordinates (r, R, τ) used to describe the vibrations of HSO/HOS. M is the center-of-mass of the SO moiety. The molecule-fixed axis system xyz is right-handed, and its origin is at the nuclear center of mass.

coordinates (r, R, τ), the stationary points on the A′ and A″ potential energy surfaces: The A′ and A″ minima for HSO and HSO, the transition state (TS) for the isomerization HSO ↔ HOS, and the energy maxima at the H−S−O and H−O−S linear geometries. Once we had determined these stationary

points by geometry optimization, we ran intrinsic reaction coordinate (IRC) calculations from each energy maximum or transition state to find the minimum energy path (MEP) to the equilibrium structure of either HSO or HOS. To determine a point on the X̃(Ã)-state MEP, we minimize the electronic energy of the X̃(Ã) state by optimizing R and r at a fixed value of τ (Figure 1). That is, the MEP describes a molecule bending (or isomerizing) with "relaxing" bond lengths and it is defined by the two functions $R_{MEP}^{(\sigma)}(\tau)$ and $r_{MEP}^{(\sigma)}(\tau)$ [$\sigma = \tilde{X}$ or $\tilde{A}$] that yield the optimized R and r values, respectively, for a given value of τ. Having determined the X̃- and Ã-state MEPs, we selected 26 discrete τ-values, $\tau_k^{(ref)}$ ($k = 1, 2, ..., 26$), in the range from $\tau = 0°$ (corresponding to the H−S−O linear geometry) to $\tau = 180°$ (corresponding to the H−O−S linear geometry). At each of these 26 values of τ, we mapped the potential energy surface in the vicinity of the MEP-points $(R_{MEP}^{(\sigma)}(\tau_k^{(ref)})$, $r_{MEP}^{(\sigma)}(\tau_k^{(ref)})$, $\tau_k^{(ref)})$ [$\sigma = \tilde{X}$ or $\tilde{A}$] by calculating a set of ab initio points at geometries with $\tau = \tau_k^{(ref)}$ but with R and r displaced from $R_{MEP}^{(\sigma)}(\tau_k^{(ref)})$ and $r_{MEP}^{(\sigma)}(\tau_k^{(ref)})$, respectively. Following this procedure, we ended up with an ab initio data set of 2 × 1147 points, i.e., 1147 points on each of the X̃ ^{2}A″ and Ã ^{2}A′ surfaces. The ab initio points are placed around the MEP in an R-interval of about ±0.1 Å and an r-interval of about ±0.2 Å.

Geometry and energies calculated for the stationary points on the X̃ ^{2}A″ and Ã ^{2}A′ potential energy surfaces are shown in Table 1, and the τ-dependent potential energy curves along the respective MEPs are shown in Figure 3 for the X̃ ^{2}A″ and Ã ^{2}A′ electronic states. At the end points, that is, for $\tau = 0$ and 180°, the X̃ ^{2}A″ and Ã ^{2}A′ Renner-split potential energy surfaces converge to a doubly degenerate $^2\Pi$ linear transition state.

For HSO, it should be noted that although the doubly degenerate energy at $\tau = 0°$ in Figure 3 corresponds to a transition state common to the two bending MEPs, at energies just below this transition state (that is, at small τ values between 2° and 11°, corresponding to the bond angle ∠(H−S−O) decreasing from 177.7° to 167.5°), the X̃-state bending MEP has a "fork" in it: One of the walls of the IRC valley changes into a slope that opens without energy barrier into a local valley with longer H−M distances of about 4.3 Å (corresponding to H−S distances of about 3.7 Å). In this valley, the molecule can

Table 1. Stationary Points on the X̃ ^{2}A″ and Ã ^{2}A′ Potential Energy Surfaces of HSO/HOS, Calculated by the Core-Valence MR-SDCI+Q/[aug-cc-pCVQZ(S,O),aug-cc-pVQZ(H)] Method

stationary point[a]	τ[b] (deg)	r(S−O)[b] (Å)	r(H−M)[b] (Å)	r(H−X)[c] (Å)	∠(H−X−Y)[d] (deg)	ΔE[e] (cm^{-1})
			X̃ ^{2}A″ Potential Energy Surface			
TS at linear HSO ($^2\Pi$)	0.0	1.5692	1.8565	1.3332	180.0	35662
HSO minimum	57.1	1.4940	1.5632	1.3589	104.9	0
TS (HSO ↔ HOS)	107.4	1.6517	1.1639	1.4291	51.0	17224
HOS minimum	146.5	1.6311	1.6593	0.9622	108.0	809
TS at linear HOS ($^2\Pi$)	180.0	1.5793	1.9970	0.9444	180.0	12133
			Ã ^{2}A′ Potential Energy Surface			
TS at linear HSO ($^2\Pi$)	0.0	1.5692	1.8565	1.3332	180.0	35662
HSO minimum	64.5	1.6501	1.4802	1.3388	93.7	14654
TS (HSO ↔ HOS)	106.1	1.6737	1.1844	1.4426	52.1	21874
HOS minimum	147.3	1.6577	1.6849	0.9618	109.0	5175
TS at linear HOS ($^2\Pi$)	180.0	1.5793	1.9970	0.9444	180.0	12133

[a]TS is a transition state. At the linear-H−S−O and linear-H−O−S TSs, the potential energy surfaces are doubly degenerate as $^2\Pi$. [b]τ is the H−M−S angle; r(S−O) and r(H−M) are the S−O and H−M distances, respectively. See Figure 1 for definitions. [c]r(H−X) is the H−S distance in the HSO region including the TS (HSO ↔ HOS), and the H−O distance in the HOS region. [d]∠(H−X−Y) = ∠(H−S−O) in the HSO region including the TS (HSO ↔ HOS), and ∠(H−X−Y) = ∠(H−O−S) in the HOS region. [e]Energy relative to the global minimum (i.e., the energy at the X̃ ^{2}A″ HSO equilibrium structure).

be described as an H⋯SO complex (correlating with $^2\Sigma^-$ at the linear limit). After passing this "bifurcated" region, the MEP regains the valley in which the energy decreases until the HSO equilibrium structure is reached. The Ã-state bending MEP has a similar, but smaller, "forked" region for τ between 2° and 3° (i.e., for 177.7° ≥ ∠(H−S−O) ≥ 176.6°). Here, the bending MEP forks out to a downward slope leading to an H⋯SO complex with an H−M distance of about 3.91 Å, corresponding to an H−S distance of about 3.41 Å (correlating with $^2\Delta$ at the linear limit). After this small bifurcated region, the bending MEP again becomes a single valley that leads the molecule to the Ã ^{2}A′ HSO equilibrium structure. In the HOS region, the bending MEPs of both the X̃ ^{2}A″ and Ã ^{2}A′ states behave normally; each of the two MEPs connects the H−O−S linear structure at τ = 180° with the respective HOS equilibrium structure without any bifurcation. Also, all bending MEP segments connecting the HSO ↔ HOS transition state with the respective equilibrium structure behave normally: They are exclusively downhill in energy. In the bifurcated regions on the X̃ ^{2}A″ and Ã ^{2}A′ potential energy surfaces for HSO, the energies and geometries of the steepest-descent path for bending motion are determined by interpolation between ab initio values obtained at τ = 0° and at $\tau \geq$ 15° along the MEP.

The dipole moment values at the equilibrium structures, calculated as the finite electric-field derivative of the MR-SDCI +Q energy, for the HSO X̃ ^{2}A″(Ã ^{2}A′) states are $\mu_{e,y}$ = 0.801(0.935) D and $\mu_{e,z}$ = −2.156(−1.136) D, respectively [with a total length of the dipole moment vector of $|\mu_e|$ = 2.300(1.472) D]. The corresponding values for the HOS X̃ ^{2}A″(Ã ^{2}A′) states are $\mu_{e,y}$ = 1.457(1.454) D and $\mu_{e,z}$ = 0.666(0.370) D, respectively [$|\mu_e|$ = 1.602(1.500) D]. The y and z coordinate axes are defined in Figure 1.

All electronic structure calculations of the present work were carried out using the MOLPRO 2010.1 suite of programs.[44]

As described in the following, the ab initio values were subsequently fitted to analytical, parametrized functions and the parameters of these functions were used as input for the variational DR program in calculations of the rovibronic energy levels of HSO/HOS.

ROVIBRONIC THEORY

The theoretical model used in the present work is described in detail by Odaka et al.[16,17] The reader is referred to these references and to Odaka's Ph.D. dissertation[15] which gives extensive details, such as explicit expressions for many matrix elements. The theory is implemented in the DR program,[15−17] which determines the eigenvalues and eigenfunctions of the rovibronic Hamiltonian $\hat{H}_{DR}$ in a standard variational calculation: The matrix representation of $\hat{H}_{DR}$ is constructed in terms of suitable basis functions[15,16] and diagonalized numerically.

For HSO/HOS, the eigenstates of $\hat{H}_{DR}$ are labeled by the good quantum numbers J, M_J, S, and Γ_{rve}, where the quantum number J pertains to the operator $\hat{J}^2 = (\hat{N} + \hat{S})^2$ with $\hat{N}$ as the total orbital angular momentum and $\hat{S}$ as the total electron spin, $M_J \hbar$ is the projection of $\hat{J}$ on the space-fixed Z axis (see, for example, Bunker and Jensen[45]), S is associated with $\hat{S}^2$, and Γ_{rve} is the symmetry of the eigenstate in the molecular symmetry group[45] of HSO/HOS

$$C_s(M) = \{E, E^*\} \tag{1}$$

Here, E is the identity operation and E^* is the inversion operation;[45] it inverts all nuclei and electrons in the molecular center of mass. The character table[45] of $C_s(M)$ (with the two possible irreducible representations A′ and A″) is given in Table 2.

Table 2. Character Table for the Molecular Symmetry Group $C_s(M)$

	E	E^*
A′	1	1
A″	1	−1

In terms of symmetry and labeling of states, the HSO/HOS calculations of the present work are completely analogous to the DR calculations for Ã $^2\Pi$ MgNC/MgCN previously described by Odaka et al.[15−17] Both HSO/HOS and MgNC/MgCN have the molecular symmetry group $C_s(M)$ given in eq 1. In particular, all vibrational basis functions [which depend on the Jacobi coordinates (r, R, τ) defined in Figure 1] are totally symmetric in the molecular symmetry group because the Jacobi coordinates are invariant under E^*.

ANALYTICAL POTENTIAL ENERGY SURFACES

We have explained above how, on each of the X̃ ^{2}A″ and Ã ^{2}A′ potential energy surfaces of HSO/HOS, we have calculated ab initio a total of 1147 points that can be divided into 26 "point clusters". The geometries of the points in each cluster have a common value of $\tau = \tau_k^{(ref)}$ (k = 1, 2, ..., 26), where the angle τ is defined in Figure 1, whereas their (R, r) values cluster around the point $(R_{MEP}^{(\sigma)}(\tau_k^{(ref)}), r_{MEP}^{(\sigma)}(\tau_k^{(ref)}))$ on the bending/isomerization MEP for HSO/HOS in the σ [σ = X̃ or Ã] electronic state. The points in a given cluster (identified by the index k and by σ = X̃ or Ã) are now fitted separately to the following parametrized function of R and r:

$$V_k^{(\sigma)}(r,R) = \sum_{i \geq 0, j \geq 0} F_{ijk}^{(\sigma)}(\xi_{r,k}^{(\sigma)})^i(\xi_{R,k}^{(\sigma)})^j \tag{2}$$

$$\xi_{r,k}^{(\sigma)} = 1 - \exp[-\beta_{r,k}^{(\sigma)}(r - r_{e,k}^{(\sigma)})] \tag{3}$$

and

$$\xi_{R,k}^{(\sigma)} = 1 - \exp[-\beta_{R,k}^{(\sigma)}(R - R_{e,k}^{(\sigma)})] \tag{4}$$

Here, the $F_{ijk}^{(\sigma)}$, the $\beta_{r,k}^{(\sigma)}$, and the $\beta_{R,k}^{(\sigma)}$ are all adjustable parameters, $r_{e,k}^{(\sigma)} = r_{MEP}^{(\sigma)}(\tau_k^{(ref)})$, $R_{e,k}^{(\sigma)} = R_{MEP}^{(\sigma)}(\tau_k^{(ref)})$, and $i + j \leq L$, where L is the expansion order. We made fittings with various values of L and found that the quality of the fittings improved substantially when L was increased from 2 to 3, whereas a further increase brought little improvement. We used L = 4.

To carry out a DR calculation, we must supply to DR a routine capable of computing the values of the X̃- and Ã-state potential energy functions at any (r, R, τ)-point. If it happens that a k-value exists for which $\tau = \tau_k^{(ref)}$, we can calculate the desired potential energy values directly from the functions given in eqs 2−4. For a value of τ that is not among the available $\tau_k^{(ref)}$-values, we proceed as follows: The known values of $r_{e,k}^{(\sigma)}$ and $R_{e,k}^{(\sigma)}$, respectively, are interpolated by means of cubic splines to produce values of these distances, r_e and R_e, at the actual value of τ (and for the given value of σ). We then calculate the displacements $\Delta r = r - r_e$ and $\Delta R = R - R_e$, and we can now use eqs 2−4 to compute potential energy values at

the reference angle values $\tau_k^{(\mathrm{ref})}$, and at the appropriate (r, R)-values, as $\mathcal{V}_k^{(\sigma)} = V_k^{(\sigma)}(r_{\mathrm{e},k}^{(\sigma)} + \Delta r, R_{\mathrm{e},k}^{(\sigma)} + \Delta R)$. The discrete values of $\mathcal{V}_k^{(\sigma)}$ generated in this manner are finally interpolated by cubic splines to produce the desired value of the potential energy function at the coordinate values (r, R, τ). In practice we choose for each σ-value only 21 values of $r_{\mathrm{e},k}^{(\sigma)}$, $R_{\mathrm{e},k}^{(\sigma)}$, and $\mathcal{V}_k^{(\sigma)}$ to use in the spline interpolation, because the remaining points cause an unsmooth behavior of the potential.

An alternative to the interpolation procedure described above for generating the potential energy values at an arbitrary (r, R, τ)-point would be to define a single, parametrized function of (r, R, τ) and to fit this function through all computed ab initio points simultaneously. However, because the potential energy functions considered in the present work cover a rather large volume of coordinate space (for example, on one hand, regions where the functions vary slowly and smoothly and, on the other hand, regions where they change drastically), these functions are difficult to model in such a direct manner. The chosen spline interpolation technique, where we start by modeling accurately (i.e., by means of eqs 2−4) the behavior of the potential energy functions near the MEPs, and then interpolate and extrapolate the "modeled" values to other regions of coordinate space, allows us to obtain realistic potential energy values at the points where DR needs them, at least after we have made some corrections to the functions; we describe these corrections in the following.

We have expanded the 2D analytical functions of eq 2 in terms of the Morse-type quantities of eqs 3 and 4 because such expansions obviously stay finite for $r \rightarrow \infty$ and/or $R \rightarrow \infty$, and thus they could, in principle, describe correctly the dissociation channels of the molecule. However, it turned out that in many cases, for $r < r_{\mathrm{e},k}^{(\sigma)}$ and/or $R < R_{\mathrm{e},k}^{(\sigma)}$, where we expect the potentials to have large positive values, the functions had spurious minima or "holes", often very deep ones (values of $-1000\ E_{\mathrm{h}}$ at the bottom were not uncommon). Such artificial holes occasionally appear when the fitted, analytical potential energy function is used to extrapolate the potential energy beyond the region where the ab initio energy calculations have actually been done. To remedy this unphysical situation, we introduced "ghost-points" in the fitting procedure: These points assigned a value of zero to the potential in areas where initial fittings had produced holes and in many cases, they made the holes disappear in subsequent fittings.

Even with the ghost-points, however, some holes remained at near-linear configurations. We removed these in the following manner: In general, a 1D cut through the potential energy function along r or R should be a function with a single minimum that attains very large values for r (or R) $\rightarrow 0$ and a constant, positive value for r (or R) $\rightarrow \infty$. As r (or R) increases to values above the value corresponding to the minimum, the analytical potential energy functions constructed from the results of initial fittings generally delivered energy values increasing with r (or R). If a hole is forming, the potential energy will attain a maximum value $\mathcal{V}^{(\mathrm{max})}$ at a particular value of r, for example, $r^{(\mathrm{max})}$ (or at $R = R^{(\mathrm{max})}$), and then it will start decreasing for further increases in r (or R). We can prevent this unphysical behavior (which is an artifact caused by the fact that we have only a limited number of ab initio points to fit) by simply assigning the value $\mathcal{V}^{(\mathrm{max})}$ to the analytical potential energy function for $r > r^{(\mathrm{max})}$ (or $R > R^{(\mathrm{max})}$). This empirical correction causes the fundamental vibrational wavenumbers of

HSO/HOS to shift by about 0.02 cm^{-1}. An example of the correction of the $\tilde{X}\ ^2A''$-state potential is given in Figure 2. This
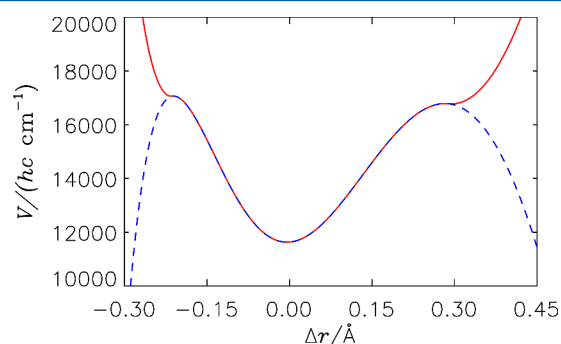

Figure 2. Correction of the $\tilde{X}\ ^2A''$ potential energy function at dissociation (see text). The figure shows cuts through the original potential energy function (blue dashed curve) and the corrected one (red full curve) around the MEP for $\tau = 175.3°$. For $\Delta r = 0$, the R and r values are such that the geometry is on the MEP; otherwise, R and r are displaced by equal amounts, $\Delta R = \Delta r$, from their respective MEP values.

figure shows cuts through the original potential energy function, and the corrected one, around the MEP for $\tau = 175.3°$. For $\Delta r = 0$, the R and r values are such that the geometry is on the MEP; otherwise, R and r are displaced by equal amounts, $\Delta R = \Delta r$, from their respective MEP values.

We have pointed out above that we sometimes encounter unphysical behavior of the analytical potential energy function when we extrapolate it beyond the region where the ab initio points are calculated, and we have described how we have endeavored to remedy the associated problems in various ways. Clearly, a more straightforward way of avoiding unphysical variation of the analytical potetial energy function would be to calculate a larger number of ab initio points, covering a larger region of vibrational-coordinate space. This was deemed computationally prohibitive in the case of HSO/HOS and so we have resorted to the more inventive approaches described above.

One-Dimensional Analysis. To get an overview of the energetics in the $\tilde{X}\ ^2A''$ and $\tilde{A}\ ^2A'$ electronic states of HSO/HOS, we consider first the bending MEPs of these two states. We plot the MEP energies as functions of τ in Figure 3 and the τ-dependences of the distances R and r along the MEPs in Figure 4. Figure 3 shows that the lowest energy (which we take as the energy zero) is attained at the HSO equilibrium configuration in the $\tilde{X}$-state, for which $\tau = 57.1°$. The $\tilde{X}$-state equilibrium configuration for HOS (with $\tau = 146.5°$) is at 809 cm^{-1} higher energy. The potential energy barrier separating the two $\tilde{X}$-state minima has a height of 17 224 cm^{-1}; the top of this barrier corresponds to $\tau = 107.4°$. Owing to the Renner degeneracies, the linear H−S−O ($\tau = 0°$) and H−O−S ($\tau = 180°$) configurations have optimized energies of 35 662 and 12 133 cm^{-1}, respectively, in both electronic states. In the $\tilde{A}$ electronic state, the HSO equilibrium configuration is found at an energy of 14 654 cm^{-1} (relative to the HSO equilibrium configuration in the $\tilde{X}$ electronic state) and it corresponds to a τ-value of 64.5°. The corresponding $\tilde{A}$-state equilibrium configuration for HOS has an energy of 5175 cm^{-1} at $\tau = 147.3°$. The top of the barrier separating the two $\tilde{A}$-state minima corresponds to an energy of 21 874 cm^{-1} (again relative to the HSO equilibrium configuration in the $\tilde{X}$
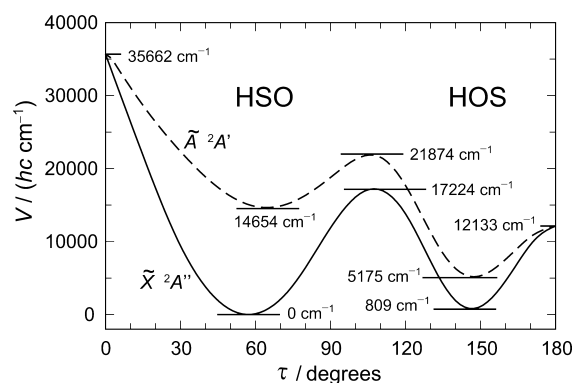
Figure 3. $\tilde{X}\ ^2A''$ and $\tilde{A}\ ^2A'$ potential energy curves along the respective bending MEPs. Extremal points are indicated. The energies of $\tilde{X}$- and $\tilde{A}$-state HSO potential energy curves near the linear transition state at $\tau = 0°$ (that is, $2° \leq \tau \leq 11°$) are those of the steepest descent path interpolated along the bending MEP (see the section Ab Initio Calculations for details).

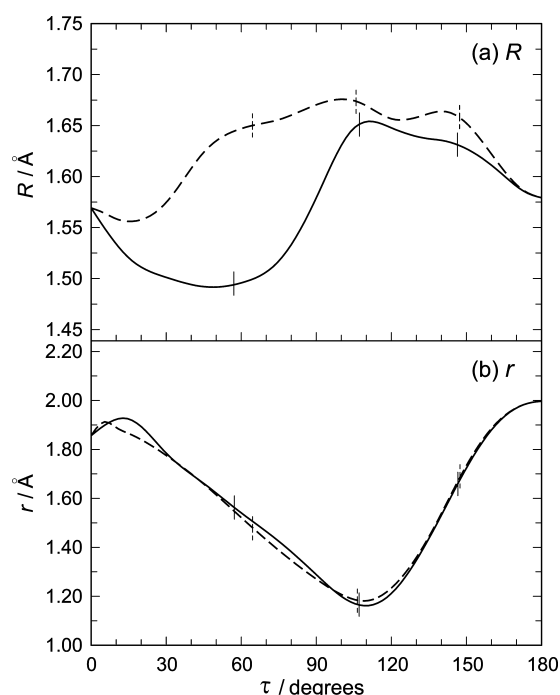**Figure 4.** τ-dependence of the distances (a) R and (b) r along the bending/isomerization MEPs in the $\tilde{X}\ ^2A''$ (solid curve) and $\tilde{A}\ ^2A'$ (dashed curve) electronic states of HSO/HOS. The data plotted in the τ-interval between (approximately) 2° and 11° are those of the steepest-descent path interpolated along the bending MEP (see the section Ab Initio Calculations for details).

Figure 5. Potential energy curve along the bending/isomerization MEP in the $\tilde{X}\ ^2A''$ electronic state of HSO/HOS, plotted in the 0–5000 cm^{-1} energy region together with the 1D bending/isomerization wave functions obtained by Numerov–Cooley solution[46,47] of the bending/isomerization Schrödinger equations associated with the MEP potential energy curves (Figure 3). The wave functions $\psi_i(\tau)$ are plotted as curves $E_i + \mathcal{K}\psi_i(\tau)$, where E_i is the bending/isomerization energy associated with the wave function $\psi_i(\tau)$ and the constant $\mathcal{K}$ has the same value for all plotted wave functions. Wave functions with dominant amplitude in the HSO(HOS) potential well are plotted as the red(blue) curve.

configurations. Hence one can say that for HOO, isomerization plays a more important role for the internal dynamics than the Renner interaction. For HSO/HOS, on the other hand, the linear H–O–S geometry has an energy below that of the isomerization barrier and so in this case, the Renner interaction plays the leading role in determining the internal dynamics.

To obtain further insight into the nature of the bending/isomerization motion of HSO/HOS, we plot in Figures 5 and 6 selected 1D bending/isomerization (i.e., τ-dependent) wave functions with $K = 0$ (see Odaka et al.[15−17]), obtained by Numerov–Cooley solution[46,47] of the bending/isomerization Schrödinger equations associated with the MEP potential energy curves in Figure 3. These functions are used as basis functions in the variational solution of the rovibronic Schrödinger equation carried out by the DR program. For the $\tilde{X}$ rovibronic states of lowest energy (Figure 5), there is no appreciable tunneling between the two potential wells, and the corresponding 1D wave functions are straightforwardly recognized as "belonging" to one of these, where it has almost all of its amplitude. These states could be satisfactorily described in an approximation where the two potential wells are considered separately. However, detailed analysis shows that even for these low-lying states, the wave functions reflect the double-well nature of the potential energy curves. For example, in the $\tilde{X}\ ^2A''$ electronic state, the lowest bending state localized in the HOS potential well can be viewed as being associated either with the bending ground state of HOS or with the first excited bending state of the "total" HSO/HOS molecule. Thus, the associated wave function is required[45] to have no nodes in the τ-interval describing HOS configurations, and one node in the complete τ-interval [0°, 180°] describing HSO/HOS. It is easily recognized from Figure 5 that the

electronic state) and a τ-value of 106.1°. The geometries of the stationary points on the potential energy surfaces are compiled in Table 1.

We note that the HSO equilibrium structure in the $\tilde{X}\ ^2A''$ electronic state is energetically well separated from the other minima. That is, if we were interested in HSO only, it would be feasible to employ a simpler approach, in which $\tilde{X}$-state HSO is considered separately, to describe its rovibronic states up to energies of at least 10 000 cm^{-1} above the equilibrium energy.

For the HOO molecule,[18] the isomerization barrier separating the two equivalent, nonlinear equilibrium geometries is lower than the barriers to the two equivalent, linear H–O–O
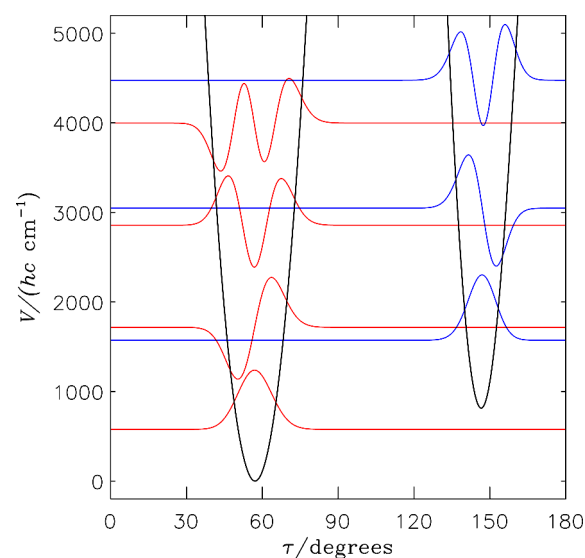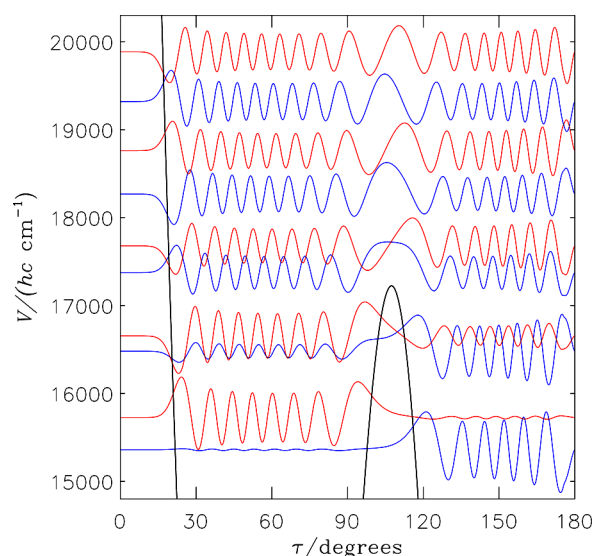
Figure 6. Potential energy curve along the bending/isomerization MEP in the $\tilde{X}\ ^2A''$ electronic state of HSO/HOS, plotted in the 15000−20000 cm^{-1} energy region together with the 1D bending/isomerization wave functions obtained by Numerov−Cooley solution[46,47] of the bending/isomerization Schrödinger equations associated with the MEP potential energy curves (Figure 3). The wave functions $\psi_i(\tau)$ are plotted as curves $E_i + \mathcal{K}\psi_i(\tau)$, where E_i is the bending/isomerization energy associated with the wave function $\psi_i(\tau)$ and the constant $\mathcal{K}$ has the same value for all plotted wave functions (and the same value as in Figure 5). The wave functions are plotted alternatingly as red and blue curves.

function has no nodes in the HOS well but the node expected outside this well is not visible in the figure. Detailed numerical analysis shows, however, that it is located near the HSO potential energy minimum.

For the states located immediately below the top of the barrier (Figure 6) separating the two $\tilde{X}$-state minima, the wave functions have the major part of their amplitude in one of the two potential wells, but they now also have substantial amplitude in the other well. This is indicative of the fact that tunneling through the barrier takes place in these states. Owing to the distribution of amplitude over the entire τ-interval [0°, 180°], all nodes of these functions are recognizable in Figure 6. At energies above the barrier maximum, the entire τ-interval becomes classically allowed, the molecule can now move rather freely between the two potential wells, and the wave function amplitude typically becomes equally shared between these. Even in these states, however, the details of the wave functions reflect the presence of the barrier: Most of the nodes are located near the two potential minima whereas nodes near the top of the barrier occur less frequently.

■ ROVIBRONIC ENERGIES

Computational Details. We have used the DR program[15−17] to compute rovibronic energies and wave functions for the $\tilde{X}\ ^2A''$ and $\tilde{A}\ ^2A'$ electronic states of HSO/HOS. These calculations are based on the analytical potential energy surfaces constructed as explained above.

The size of vibrational basis set (see Odaka et al.[15−17] for the definition of the parameters and the other quantities mentioned here) was determined by the parameter values $(\nu_2^a)^{(\text{max})} = 50$, $(\nu_2^b)^{(\text{max})} = 40$, $N_R^{(\text{max})} = 12$, and $N_r^{(\text{max})} = 5$.

For the stretching basis functions $|N_R, \Gamma_R\rangle$ and $|N_r, \Gamma_r\rangle$ we have used the parameter values $r_e = 2.912333\ a_0$ and $R_e = 2.826918\ a_0$, $D_e^{(r)} = 15\ E_h$, $D_e^{(R)} = 0.6\ E_h$, $hc\omega_e^{(r)} = 0.008\ E_h$, and $hc\omega_e^{(R)} = 0.0018\ E_h$. The number of integration points for the Gauss−Laguerre integration over the r and R coordinates were both 15. The spin−orbit interaction parameter was chosen as a τ-dependent function $A_{SO}(\tau)$ for HSO/HOS: a piecewise linear function with values obtained by averaging the ab initio results over r and R. At the HSO and HOS equilibrium structures in the $\tilde{X}\ ^2A''$ state, $A_{SO}(\tau)$ has the values −0.9 and −16.3 cm^{-1}, respectively. This large change in $A_{SO}(\tau)$ between HSO and HOS demonstrates that although the two molecules are both asymmetric, that is of type ABC, the exchange of the O and S nuclei causes a significant change in the role of the spin−orbit interaction.

The threshold energy for K-block contraction,[15−17] E_{cont}, was taken to be 30 000 cm^{-1}. The size of the bending basis set and E_{cont} are chosen to be larger here than in our previous, analogous calculations on HOO.[18] The basis set and the E_{cont}-value of the present work are sufficiently large for describing HSO−HOS isomerization for both electronic states and the Renner interaction originating at the H−O−S linear configuration.

In practice, we do not calculate the effects of the Renner interaction originating at the H−S−O linear structure. This structure is located at 35 662 cm^{-1} above the HSO potential minimum in the $\tilde{X}\ ^2A''$ state; in the states associated with the energies calculated in the present work, this geometry is inaccessible to the molecule. At such a large potential energy, our potential energy surface for the HSO $\tilde{X}\ ^2A''$ state is not well-defined owing to the bifurcation mentioned in the section Ab Initio Calculations above, and an accurate calculation of the rovibronic energies in this energy region is not possible at the present time.

Results. The calculated fundamental vibrational wavenumbers of the HSO and HOS molecules in the $\tilde{X}\ ^2A''$ and $\tilde{A}\ ^2A'$ electronic states are listed in Table 3 where they are compared with the available, experimentally derived values[38,39] and with the CCSD(T) ab initio values from Wang and Wilson.[29] The experimentally derived ν_3 term value for $\tilde{X}\ ^2A''$ HSO is highly accurate; it is obtained by the technique of

Table 3. Calculated Fundamental Term Values of HSO/HOS (cm^{-1})

state	minimum		present work	exp[38,39]	CCSD(T)[29]
$\tilde{X}\ ^2A''$	HSO	ν_3	1024.85	1009.3551(10)[a,b]	1027
$\tilde{X}\ ^2A''$	HSO	ν_2	1087.79	1079(3)[c]	1102
$\tilde{X}\ ^2A''$	HSO	ν_1	2415.31	2325(3)[c]	2448
$\tilde{X}\ ^2A''$	HOS	ν_3	863.25		851
$\tilde{X}\ ^2A''$	HOS	ν_2	1189.90		1200
$\tilde{X}\ ^2A''$	HOS	ν_1	3652.12		3791
$\tilde{A}\ ^2A'$	HOS	ν_3	790.63		
$\tilde{A}\ ^2A'$	HOS	ν_2	1073.08		
$\tilde{A}\ ^2A'$	HOS	ν_1	3775.25		
$\tilde{A}\ ^2A'$	HSO	ν_3	745.27	703.497(19)[d]	
$\tilde{A}\ ^2A'$	HSO	ν_2	842.41	784.029(11)[d]	
$\tilde{A}\ ^2A'$	HSO	ν_1	2556.75		

[a]From Sears and McKellar.[38] [b]Quantities in parentheses are quoted uncertainties in units of the last digit given. [c]From Table 3 of Yoshikawa et al.[39] [d]Calculated from the values of the parameters ω_2, ω_3, and x_{33} given in Table 6 of Yoshikawa et al.[39]

Table 4. Calculated Term Values E/hc (cm^{-1}) for the $J = 1/2$, $N_{K_aK_c} = 0_{00}$ Levels of $\tilde{X}\,^2A''$ and $\tilde{A}\,^2A'$ HSO/HOS up to 8277.17 cm^{-1} above the Vibronic Ground State Given Together with the Probabilities P_+ and P_{HSO} of Finding the Molecule in the $\tilde{A}\,^2A'$ State and in the H−S−O Configuration, Respectively, and the Rovibrational Symmetry Label Γ_{rve} (See Text)

state	E_{calc}	E_{exp}[39]	Γ_{rve}	P_+	P_{HSO}	state	E_{calc}	Γ_{rve}	P_+	P_{HSO}
$\tilde{X}\,^2A''$ (0,0,0) HSO	0.00		A′	0.00	1.00		6266.39	A′	0.00	1.00
$\tilde{X}\,^2A''$ (0,0,1) HSO	1024.85	1011.(5)	A′	0.00	1.00		6295.10	A′	0.00	0.00
$\tilde{X}\,^2A''$ (0,1,0) HSO	1087.79	1084.(5)	A′	0.00	1.00		6373.44	A′	0.00	1.00
$\tilde{X}\,^2A''$ (0,0,0) HOS	1409.71		A′	0.00	0.00		6468.67	A′	0.00	1.00
$\tilde{X}\,^2A''$ (0,0,2) HSO	2042.23	2004.(5)	A′	0.00	1.00		6469.12	A′	0.00	0.00
$\tilde{X}\,^2A''$ (0,1,1) HSO	2109.92	2078.(5)	A′	0.00	1.00		6472.93	A′	0.00	1.00
$\tilde{X}\,^2A''$ (0,2,0) HSO	2171.93		A′	0.00	1.00	$\tilde{A}\,^2A'$ (0,0,1) HOS	6480.51	A″	1.00	0.00
$\tilde{X}\,^2A''$ (0,0,1) HOS	2272.96	2323.(5)	A′	0.00	0.00		6542.38	A′	0.00	1.00
$\tilde{X}\,^2A''$ (1,0,0) HSO	2415.31		A′	0.00	1.00		6576.40	A′	0.00	0.00
$\tilde{X}\,^2A''$ (0,1,0) HOS	2599.61		A′	0.00	0.00		6622.41	A′	0.00	1.00
$\tilde{X}\,^2A''$ (0,0,3) HSO	3053.18	2996.(5)	A′	0.00	1.00		6635.07	A′	0.00	1.00
$\tilde{X}\,^2A''$ (0,1,2) HSO	3127.92	3060.(5)	A′	0.00	1.00		6708.83	A′	0.00	1.00
$\tilde{X}\,^2A''$ (0,0,2) HOS	3138.77		A′	0.00	0.00	$\tilde{A}\,^2A'$ (0,1,0) HOS	6762.96	A″	1.00	0.00
$\tilde{X}\,^2A''$ (0,2,1) HSO	3193.17		A′	0.00	1.00		6767.42	A′	0.00	1.00
$\tilde{X}\,^2A''$ (0,3,0) HSO	3254.06		A′	0.00	1.00		6824.89	A′	0.00	1.00
$\tilde{X}\,^2A''$ (1,0,1) HSO	3442.36		A′	0.00	1.00		6834.95	A′	0.00	0.00
$\tilde{X}\,^2A''$ (0,1,1) HOS	3457.31		A′	0.00	0.00		6881.72	A′	0.00	1.00
$\tilde{X}\,^2A''$ (1,1,0) HSO	3489.25	3967.(3)	A′	0.00	1.00		6940.85	A′	0.00	1.00
$\tilde{X}\,^2A''$ (0,2,0) HOS	3813.06		A′	0.00	0.00		6952.59	A′	0.00	0.00
$\tilde{X}\,^2A''$ (0,0,3) HOS	4036.55	4030.(3)	A′	0.00	0.00		6957.94	A′	0.00	1.00
$\tilde{X}\,^2A''$ (0,0,4) HSO	4063.05		A′	0.00	1.00		7084.91	A′	0.00	1.00
$\tilde{X}\,^2A''$ (0,1,3) HSO	4145.23		A′	0.00	1.00		7162.62	A′	0.00	0.00
$\tilde{X}\,^2A''$ (0,2,2) HSO	4229.29		A′	0.00	1.00		7170.97	A′	0.00	1.00
$\tilde{X}\,^2A''$ (0,3,1) HSO	4304.08		A′	0.00	1.00		7192.55	A′	0.00	1.00
$\tilde{X}\,^2A''$ (0,1,2) HOS	4318.58		A′	0.00	0.00	$\tilde{A}\,^2A'$ (0,0,2) HOS	7276.01	A″	1.00	0.00
	4344.63		A′	0.00	1.00		7277.02	A′	0.00	1.00
	4455.50		A′	0.00	1.00		7365.86	A′	0.00	0.00
	4522.07		A′	0.00	1.00		7397.61	A′	0.00	1.00
	4563.90		A′	0.00	1.00		7477.27	A′	0.00	1.00
$\tilde{X}\,^2A''$ (0,2,1) HOS	4672.42		A′	0.00	0.00		7487.28	A′	0.00	0.00
	4741.27		A′	0.00	1.00		7512.23	A′	0.00	1.00
$\tilde{X}\,^2A''$ (1,0,0) HOS	5061.83		A′	0.00	0.00		7513.13	A′	0.00	0.00
$\tilde{X}\,^2A''$ (0,0,4) HOS	5071.43		A′	0.00	0.00	$\tilde{A}\,^2A'$ (0,1,1) HOS	7549.67	A″	1.00	0.00
	5074.38		A′	0.00	1.00		7553.54	A′	0.00	1.00
$\tilde{X}\,^2A''$ (1,1,0) HOS	5151.72		A′	0.00	0.00		7624.16	A′	0.00	1.00
	5156.91		A′	0.00	1.00		7644.87	A′	0.00	1.00
$\tilde{X}\,^2A''$ (0,1,3) HOS	5214.98		A′	0.00	0.00		7691.59	A′	0.00	0.00
	5250.36		A′	0.00	1.00		7740.22	A′	0.00	1.00
	5341.97		A′	0.00	1.00		7770.06	A′	0.00	0.00
	5413.85		A′	0.00	1.00		7812.59	A′	0.00	1.00
	5464.06		A′	0.00	1.00		7859.55	A′	0.00	1.00
	5536.61		A′	0.00	1.00		7906.67	A′	0.00	0.00
$\tilde{X}\,^2A''$ (0,2,2) HOS	5540.28		A′	0.00	0.00	$\tilde{A}\,^2A'$ (0,2,0) HOS	7928.65	A″	1.00	0.00
	5595.75		A′	0.00	1.00		7937.99	A′	0.00	1.00
	5638.33		A′	0.00	1.00		7964.09	A′	0.00	1.00
	5670.17		A′	0.00	1.00		7996.50	A′	0.00	1.00
$\tilde{A}\,^2A'$ (0,0,0) HOS	5689.88		A″	1.00	0.00		8046.79	A′	0.00	0.00
	5798.42		A′	0.00	1.00		8074.20	A′	0.00	1.00
	5819.64		A′	0.00	1.00		8091.04	A′	0.00	1.00
	5947.94		A′	0.00	0.00		8093.97	A′	0.00	0.00
	6043.12		A′	0.00	0.00	$\tilde{A}\,^2A'$ (0,0,3) HOS	8101.84	A″	1.00	0.00
	6083.76		A′	0.00	1.00		8137.09	A′	0.00	1.00
	6165.39		A′	0.00	1.00		8167.21	A′	0.00	0.00
	6182.82		A′	0.00	0.00		8171.15	A′	0.00	1.00
	6242.78		A′	0.00	0.00		8277.17	A′	0.00	1.00

intracavity CO_2 laser magnetic resonance.[38] The remaining experimentally derived values are obtained from partly resolved dispersed fluorescence spectra[39] and are somewhat less accurate. Our calculation reproduces fairly well the exper-

Table 5. Calculated Term Values E/hc (cm^{-1}) for the $J = 1/2$, $N_{K_aK_c} = 0_{00}$ Levels of X̃ ^{2}A″ and Ã ^{2}A′ HSO/HOS in the Range 8282.54−18522.64 cm^{-1} above the Vibronic Ground State Given Together with the Probabilities P_+ and P_{HSO} of Finding the Molecule in the Ã ^{2}A′ State and in the H−S−O Configuration, Respectively, and the Rovibrational Symmetry Label Γ_{rve} (See Text)

state	E_{calc}	Γ_{rve}	P_+	P_{HSO}	state	E_{calc}	Γ_{rve}	P_+	P_{HSO}	E_{calc}	Γ_{rve}	P_+	P_{HSO}
	8282.54	A′	0.00	1.00		9923.57	A′	0.00	1.00	17877.15	A′	0.00	0.93
Ã ^{2}A′ (0,1,2) HOS	8347.73	A″	1.00	0.00	Ã ^{2}A′ (0,3,1) HOS	9950.96	A″	1.00	0.00	17895.15	A″	0.98	0.00
	8410.53	A′	0.00	0.00		9966.42	A′	0.00	1.00	17917.75	A′	0.02	0.05
	8413.82	A′	0.00	1.00		...				17929.15	A′	0.00	0.95
	8484.08	A′	0.00	1.00		10072.22	A′	0.00	1.00	17948.22	A′	0.00	0.92
	8542.43	A′	0.00	1.00	X̃ ^{2}A″ (0,1,7) HOS	10086.67(a)	A′	0.01	0.00	17976.03	A′	0.00	0.86
	8556.94	A′	0.00	0.00		10092.13	A″	0.98	0.00	17995.97	A′	0.00	0.30
	8564.96	A′	0.00	1.00		10137.89	A′	0.00	1.00	18018.50	A″	0.91	0.08
	8574.36	A′	0.00	1.00		...				18018.97	A′	0.35	0.58
	8612.71	A′	0.00	0.00		10265.52	A′	0.00	1.00	18034.81	A′	0.01	0.17
	8661.06	A′	0.00	1.00	Ã ^{2}A′ (1,0,1) HOS	10297.56	A″	1.00	0.00	18037.10	A′	0.00	0.84
	8668.96	A′	0.00	1.00		10298.28	A′	0.00	1.00	18053.64	A′	0.00	0.82
	8703.57	A′	0.00	1.00		10359.38	A′	0.00	1.00	18067.62	A′	0.00	0.97
Ã ^{2}A′ (0,2,1) HOS	8719.18	A″	1.00	0.00	Ã ^{2}A′ (0,4,0) HOS	10374.27	A″	1.00	0.00	18092.62	A′	0.00	0.90
	8771.47	A′	0.00	1.00		10396.40	A″	1.00	0.00	18104.42	A″	1.00	1.00
	8798.28	A′	0.00	0.00		...				18107.40	A′	0.01	0.18
	8841.85	A′	0.00	0.00		12255.87	A′	0.03	0.00	18118.75	A′	0.00	0.14
	8870.69	A′	0.00	1.00		12257.55	A″	0.58	0.00	18123.14	A′	0.00	0.95
	8895.56	A′	0.00	1.00		12295.30	A′	0.00	0.00	18124.43	A″	0.90	0.09
	8987.35	A′	0.00	1.00		...				18145.06	A′	0.01	0.88
	8991.14	A′	0.00	0.00		13408.65	A′	0.00	1.00	18152.53	A″	0.96	0.02
	9010.71	A′	0.00	1.00	X̃ ^{2}A″ (1,10,0) HSO	13423.96(b)	A′	0.00	0.98	18172.12	A′	0.00	0.93
	9018.82	A′	0.00	0.00		13425.42	A′	0.00	0.02	18180.72	A″	1.00	0.01
Ã ^{2}A′ (0,0,4) HOS	9024.05	A″	1.00	0.00		...				18183.67	A′	0.01	0.59
	9050.40	A′	0.00	1.00		14447.89	A′	1.00	0.00	18194.30	A′	0.01	0.41
	9063.18	A′	0.00	0.00	Ã ^{2}A′ (0,0,0) HSO	14461.92	A″	1.00	1.00	18205.18	A′	0.00	0.90
	9082.00	A′	0.00	1.00		14510.64	A′	0.00	1.00	18225.91	A′	0.00	0.46
	9084.89	A′	0.00	0.00		...				18259.32	A′	0.00	0.60
	9104.10	A′	0.00	1.00	Ã ^{2}A′ (0,0,1) HSO	15207.19	A″	1.00	1.00	18277.87	A″	1.00	1.00
	9159.67	A′	0.00	1.00		...				18289.55	A″	0.99	0.00
Ã ^{2}A′ (0,3,0) HOS	9160.46	A″	1.00	0.00	Ã ^{2}A′ (0,1,0) HSO	15304.33	A″	1.00	1.00	18290.39	A′	0.01	0.96
	9164.83	A′	0.00	1.00		...				18300.94	A′	0.00	0.94
Ã ^{2}A′ (0,1,3) HOS	9171.74	A″	1.00	0.00	Ã ^{2}A′ (0,0,2) HSO	15946.12	A″	1.00	1.00	18303.01	A′	0.00	0.28
	9263.11	A′	0.00	0.00		...				18326.03	A′	0.00	0.97
	9273.50	A′	0.00	1.00	Ã ^{2}A′ (0,1,1) HSO	16042.63	A″	1.00	1.00	18328.88	A′	0.44	0.02
	9279.15	A′	0.00	1.00		...				18335.67	A″	0.53	0.01
	9370.99	A′	0.00	1.00	Ã ^{2}A′ (0,2,0) HSO	16138.81	A″	1.00	1.00	18357.48	A′	0.00	0.88
	9394.94	A′	0.00	1.00		...				18362.27	A′	0.00	0.51
	9421.17	A′	0.00	1.00	Ã ^{2}A′ (0,0,3) HSO	16669.41	A″	1.00	1.00	18372.93	A″	1.00	0.00
	9433.01	A′	0.00	0.00		...				18391.48	A′	0.00	0.90
Ã ^{2}A′ (1,0,0) HOS	9465.13	A″	1.00	0.00	Ã ^{2}A′ (0,1,2) HSO	16795.01	A″	1.00	1.00	18400.26	A′	0.00	0.90
	9486.09	A′	0.00	0.00		...				18408.04	A′	0.00	0.87
	9490.91	A′	0.00	1.00	Ã ^{2}A′ (0,2,1) HSO	16866.86	A″	1.00	1.00	18417.64	A″	1.00	1.00
	9502.92	A′	0.00	1.00		...				18430.27	A″	0.90	0.04
Ã ^{2}A′ (0,2,2) HOS	9537.65	A″	1.00	0.00	Ã ^{2}A′ (0,3,0) HSO	16960.08	A″	1.00	1.00	18436.50	A′	0.21	0.21
	9565.96	A′	0.00	1.00		...				18452.57	A′	0.00	0.95
	9585.46	A′	0.00	1.00	Ã ^{2}A′ (1,0,0) HSO	17018.67	A″	1.00	1.00	18484.81	A″	0.96	0.01
	9638.36	A′	0.00	0.00		...				18488.11	A′	0.07	0.68
	9693.68	A′	0.00	1.00	Ã ^{2}A′ (0,0,4) HSO	17389.33	A″	1.00	1.00	18494.31	A′	0.03	0.33
	9705.27	A′	0.00	1.00		...				18494.62	A′	0.00	0.79
	9717.71	A′	0.00	1.00	Ã ^{2}A′ (0,1,3) HSO	17551.48	A″	1.00	1.00	18507.85	A″	1.00	1.00
	9743.03	A′	0.00	0.00		...				18508.03	A′	0.00	0.97
	9820.87	A′	0.00	1.00	Ã ^{2}A′ (1,0,1) HSO	17791.19	A″	1.00	1.00	18509.00	A″	1.00	1.00
	9840.20	A′	0.00	0.00		...				18511.41	A″	0.98	0.02
	9921.93	A′	0.00	0.00	Ã ^{2}A′ (1,1,0) HSO	17861.34	A″	1.00	1.00	18522.64	A′	0.02	0.51

imentally derived fundamental term values for the ν_2 and ν_3 states of X̃ ^{2}A″ HSO, and our results are at least in broad agreement with the experimentally derived fundamental term

values for the ν_2 and ν_3 states of Ã ^{2}A′ HSO. It is remarkable, however, that the ab initio potential energy surfaces of the present work produce a value of the ν_1 fundamental term value
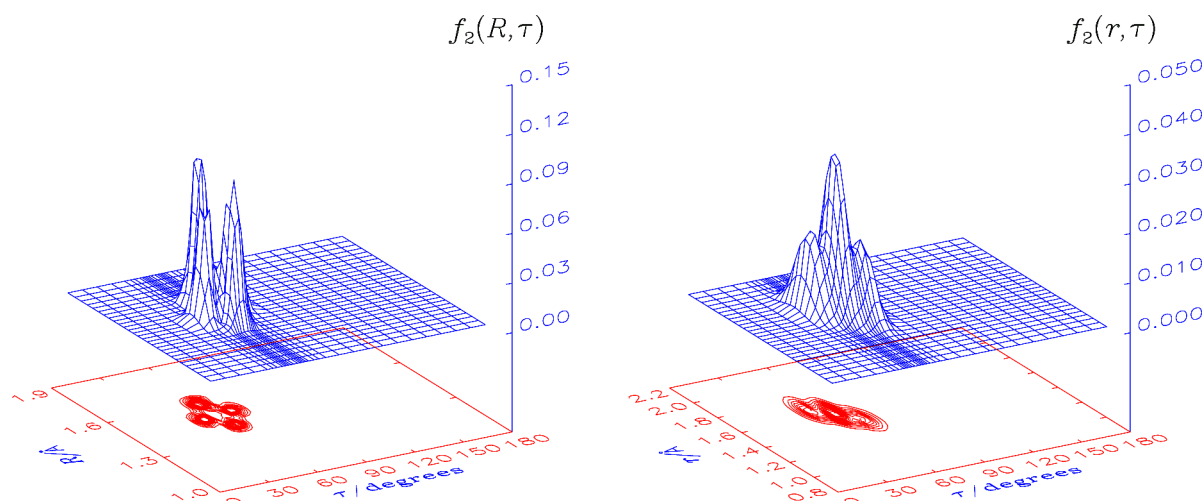
Figure 7. Functions $f_2(R,\tau)$ and $f_2(r,\tau)$ (in units of Å^{-1}) for the $\tilde{X}(0,1,1)$ HSO, $J = 1/2$ state with term value 2109.92 cm^{-1}.

of $\tilde{X}\ ^2A''$ HSO that is almost 100 cm^{-1} larger than the experimentally derived result. We note (Table 3) that the CCSD(T) ab initio calculation of Wang and Wilson[29] has the same problem, and an RCCSD(T) ab initio calculation carried out by Yoshikawa et al.[39] gave a value of 2443 cm^{-1}, close to the result of Wang and Wilson[29] (2448 cm^{-1}; Table 3) and more than 100 cm^{-1} larger than the experimentally derived value. The reason for this discrepancy is not understood at present.

Calculated rovibrational energy levels of HSO/HOS are listed in Tables 4 and 5; the quantum numbers labeling the states are derived from wave function analysis, chiefly in terms of the functions $f_1(\tau)$, $f_2(R,\tau)$, and $f_2(r,\tau)$ defined in the following. Such a detailed analysis of the wave functions yields a more realistic labeling of the states than the more straightforward determination of the basis function with the largest contribution to the eigenfunction, especially for $\tilde{A}(100)$ HSO/HOS states. In the tables, we also list the probabilities P_+ and P_{HSO} defined below. Table 4 comprises effectively "pure" states belonging either to HSO or to HOS, in either the $\tilde{X}\ ^2A''$ or $\tilde{A}\ ^2A'$ electronic state. However, Table 5 shows how, as the energy increases, first $\tilde{X}\ ^2A''$–$\tilde{A}\ ^2A'$ mixing (i.e., Renner interaction), and then HSO–HOS tunneling, occur.

Following Odaka et al.[15−17] and Melnikov et al.,[18] we analyze the wave functions of selected states by calculating probability distributions $f_1(\tau)$ and $f_2(r,\tau)$. The function $f_1(\tau)$ (eq 37 of Odaka et al.[16]) is defined such that the differential probability dp_1 of finding the molecule with the bending coordinate in the infinitesimal interval between τ and $\tau + d\tau$ is given as

$$dp_1 = f_1(\tau)\,d\tau \tag{5}$$

This function can be expressed as

$$f_1(\tau) = f_-(\tau) + f_+(\tau) \tag{6}$$

where $f_\sigma(\tau)\,d\tau$, $\sigma = -$ or $+$ for the $\tilde{X}\ ^2A''$ or $\tilde{A}\ ^2A'$ state, is the differential probability of finding the molecule in the Born–Oppenheimer electronic state $\psi_e^{(\sigma)}$ (i.e., $\psi_e^{(-)}$ for the $\tilde{X}\ ^2A''$ state and $\psi_e^{(+)}$ for the $\tilde{A}\ ^2A'$ state) with its bending coordinate between τ and $\tau + d\tau$. The functions $f_-(\tau)$ and $f_+(\tau)$ measure the extent of the mixing of the two electronic states $\psi_e^{(-)}$ and $\psi_e^{(+)}$ in the total rovibronic wave function at a given value of τ.

The overall probability of finding the molecule in the Born–Oppenheimer electronic state $\psi_e^{(\sigma)}$, $\sigma = -$ or $+$, is

$$P_\sigma = \int_0^\pi f_\sigma(\tau)\,d\tau \tag{7}$$

with $P_- + P_+ = 1$.

We define the overall probabilities of finding the molecule on the HSO and HOS sides of the barrier as

$$P_{HSO} = \int_0^{\tau_b} f_1(\tau)\,d\tau \quad \text{and} \quad P_{HOS} = \int_{\tau_b}^\pi f_1(\tau)\,d\tau \tag{8}$$

respectively, where τ_b is the value of τ at the top of the potential barrier separating the HSO and HOS minima in the $\tilde{X}\ ^2A''$ state; $\tau_b = 1.875$ rad (or 107.4°). Obviously, just as for P_- and P_+, we have $P_{HSO} + P_{HOS} = 1$.

The probability density function $f_2(r,\tau)$ is given by eq 41 of Odaka et al.[16] It is defined such that

$$dp_2 = f_2(r,\tau)\,dr\,d\tau \tag{9}$$

is the differential probability of finding the molecule with the bending coordinate in the infinitesimal interval between τ and $\tau + d\tau$ and the H–M distance (Figure 1) in the interval between r and $r + dr$. Analogously, the function $f_2(R,\tau)$ is defined such that $dp_2' = f_2(R,\tau)\,dR\,d\tau$ is the differential probability of finding the molecule with the bending coordinate in the interval between τ and $\tau + d\tau$ and the S–O distance (Figure 1) in the interval between R and $R + dR$.

In Tables 4 and 5 we give the rovibronic symmetries Γ_{rve} in the $C_s(M)$ molecular symmetry group[45] and we give values of P_+ and P_{HSO}; P_- and P_{HOS} can be obtained as $1 - P_+$ and $1 - P_{HSO}$, respectively. As mentioned above, in the low-energy states both the HSO/HOS tunneling and the Renner effect are negligible, so for these states, both P_+ and P_{HSO} assume values of 0 or 1 (where, obviously, states with $P_+ = 1$ and thus $P_- = 0$ occur at energies near the $\tilde{A}$-state minimum).

At energies about 10 000 cm^{-1}, the Renner interactions become significant. The lowest state, for which $P_+ \neq 0$ or 1 when given with two decimal places, is the 10 086.67 cm^{-1}; it has $P_+ = 0.01$ and $P_{HSO} = 0.00$, we have marked it by "(a)" in Table 5. This state has significant mixing of basis states and so it is difficult to label it in the customary manner. However by visualizing the wave function in terms of the functions $f_2(r,\tau)$, $f_2(R,\tau)$, $f_1(\tau)$, $f_-(\tau)$, and $f_+(\tau)$, and by considering the energy level pattern, we obtain the approximate label $\tilde{X}\ ^2A''$ (0,1,7) HOS. As the rovibronic energy approaches the top of the
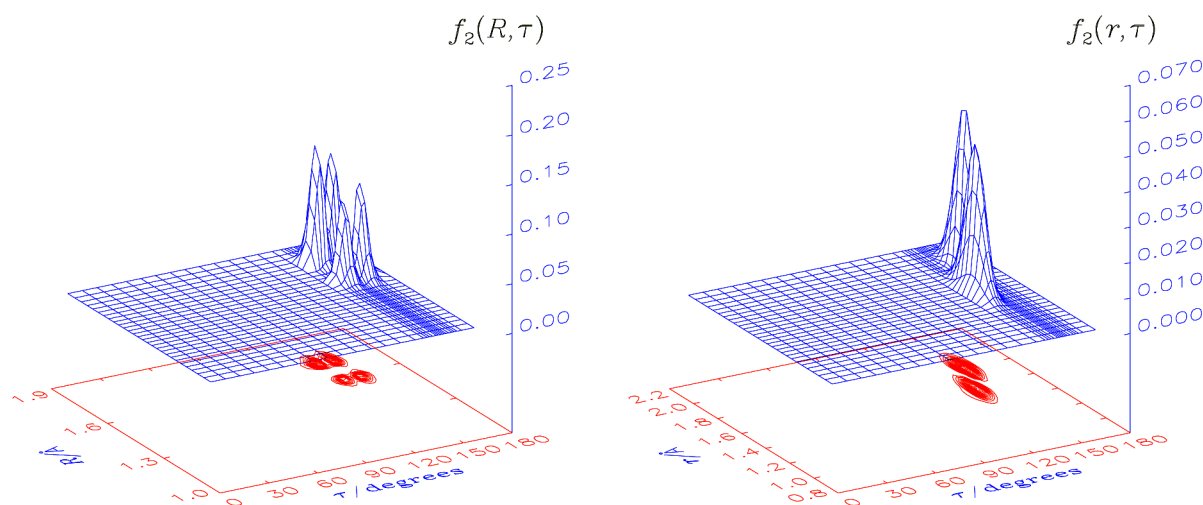
Figure 8. Functions $f_2(R,\tau)$ and $f_2(r,\tau)$ (in units of Å^{-1}) for the $\tilde{X}(0,1,1)$ HOS, $J = 1/2$ state with term value 3457.31 cm^{-1}.
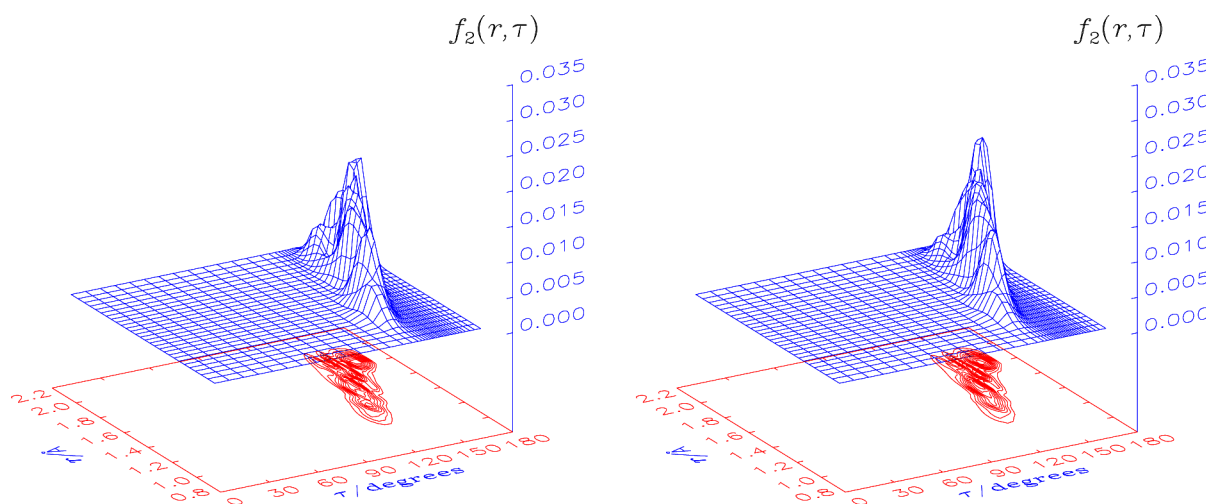

Figure 9. Function $f_2(r,\tau)$ (in units of Å^{-1}) for two $J = 1/2$ states with strong Renner interaction. Left panel: state with $N_{K_aK_c} = 1_{10}$, $\Gamma_{rve} = A''$, and $E/hc = 12\,256.69$ cm^{-1}. Right panel: state with $N_{K_aK_c} = 0_{00}$, $\Gamma_{rve} = A''$, and $E/hc = 12\,257.55$ cm^{-1}.

barrier separating the HSO and HOS potential wells in the $\tilde{X}$ $^2A''$ state, the tunneling increases. The lowest state, for which $P_{HSO} \neq 0$ or 1 when given with two decimal places, is marked by "(b)" in Table 5. It is located at 13 423.96 cm^{-1} and assigned (by combining the visualization of the wave function with the determination of the basis function with the largest contribution to the eigenfunction, and with the analysis of the energy level pattern) as $\tilde{X}$ $^2A''$ (1,10,0) HSO with $P_+ = 0$ and $P_{HSO} = 0.98$. The labels suggest that the Renner interaction is facilitated by excitation of the S−O stretching vibration whereas, as expected, significant HSO/HOS tunneling comes about exclusively by excitation of the bending mode.

At still higher energy, larger tunneling splittings occur for the states with high bending excitation.

In Figures 7−11, we visualize the wave functions of a number of selected rovibronic states of HSO/HOS in terms of the probability density functions $f_2(r,\tau)$, $f_2(R,\tau)$, $f_1(\tau)$, $f_-(\tau)$, and $f_+(\tau)$. We give examples of low-lying states, states with strong Renner interaction, and states with significant isomerization tunneling.

The functions $f_2(r,\tau)$ and $f_2(R,\tau)$ for the $\tilde{X}(0,1,1)$ HSO, $J = 1/2$ state (term value 2109.92 cm^{-1}) are shown in Figure 7, and

those for the $\tilde{X}(0,1,1)$ HOS, $J = 1/2$ state (term value 3457.31 cm^{-1}) are shown in Figure 8. The complete nodal structure of the wave functions can, in principle, be recognized from the plots of the probability density functions $f_2(r,\tau)$ and $f_2(R,\tau)$, and so these plots can be used to assign vibrational labels to the states in question. In the two states visualized in Figures 7 and 8, the r-stretch vibration is not excited but the double maxima in the R and τ directions of the $f_2(R,\tau)$ functions indicate that each of the corresponding vibrations is singly excited. The shapes of the $f_2(r,\tau)$ functions reflect that the vibration takes place predominantly along the MEP.

Figure 4 shows that the R and r coordinates vary with τ in a complicated manner along the MEP and, because of this, the $f_2(R,\tau)$ and $f_2(r,\tau)$ functions obtained for states localized in the HOS minimum are substantially different from those associated with functions localized in the HSO minimum. For example, the $f_2(R,\tau)$ for the $\tilde{X}(0,1,1)$ HSO state (Figure 7) is not simply a shifted version of the $\tilde{X}(0,1,1)$ HOS function (Figure 8); the HOS function is rotated by about 45° relative to the HSO function. Even more drastic differences are found for the HOS and HSO $f_2(r,\tau)$ functions, as exemplified by Figures 7 and 8.
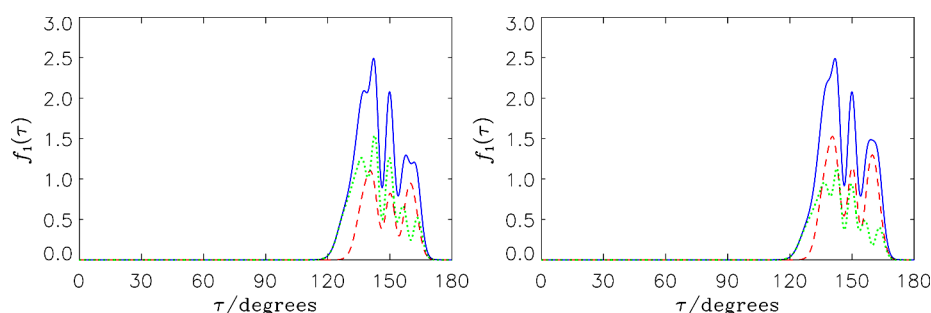
Figure 10. Functions $f_1(\tau)$ (blue solid curve), $f_-(\tau)$ (red dashed curve), and $f_+(\tau)$ (green dotted curve), all in units of rad^{-1}, for the two states visualized in Figure 9. Left panel: state with $N_{K_aK_c} = 1_{10}$, $\Gamma_{rve} = A''$, and $E/hc = 12\,256.69$ cm^{-1}. Right panel: state with $N_{K_aK_c} = 0_{00}$, $\Gamma_{rve} = A''$, and $E/hc = 12\,257.55$ cm^{-1}.
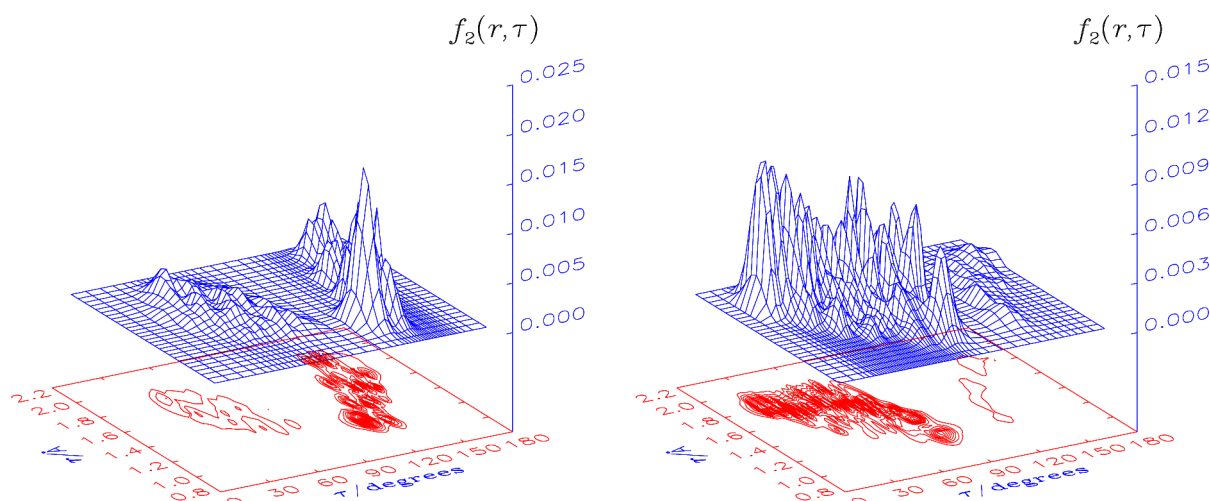

Figure 11. Functions $f_2(r,\tau)$ for two $J = 1/2$ states of HSO/HOS with significant HSO-HOS tunneling. Left panel: state with $N_{K_aK_c} = 1_{10}$, $\Gamma_{rve} = A''$, and $E/hc = 15\,647.16$ cm^{-1}. Right panel: state with $N_{K_aK_c} = 1_{11}$, $\Gamma_{rve} = A''$, and $E/hc = 15\,700.53$ cm^{-1}.

Figure 9 shows the probability density function $f_2(r,\tau)$ for two states with strong Renner interaction. These states have P_+-values of 0.42 and 0.58, respectively, and term values of 12 256.69 and 12 257.55 cm^{-1}. The one-dimensional probability density functions $f_1(\tau)$, $f_-(\tau)$, and $f_+(\tau)$ for the same two states are plotted in Figure 10. Finally, Figure 11 presents the $f_2(r,\tau)$ functions for two states with P_{HSO}-values of 0.38 and 0.85, respectively. In these states (whose term values are 15 647.16 and 15 700.53 cm^{-1}, respectively) the HSO−HOS tunneling is significant.

In Figure 12 we show a term value diagram for all states with $J \leq 13/2$ and term values in the interval 5000−20000 cm^{-1} above the rovibronic ground state. We plot the term values against the probability P_+ of finding the molecule in the $\tilde{A}\,^2A'$ state. We do not include states with term values below 5000 cm^{-1} because they all have $P_+ = 0$; below 5000 cm^{-1} there are no $\tilde{A}\,^2A'$ rovibronic basis states available for interaction with the $\tilde{X}\,^2A''$ states and so no noticeable Renner coupling occurs. Figure 13 is an analogous diagram for the same states, but the term values are plotted against the probability P_{HSO}. As the energy increases, Renner interaction becomes significant around 7500 cm^{-1} whereas HSO/HOS isomerization starts at higher energies around 12 000 cm^{-1}. This is in accordance with the one-dimensional analysis described above. In Figures 12 and 13 it is seen the points have a tendency to arrange themselves in a manner almost symmetrical with respect to the imaginary vertical lines at $P_+ = 0.5$ and $P_{HSO} = 0.5$, respectively,
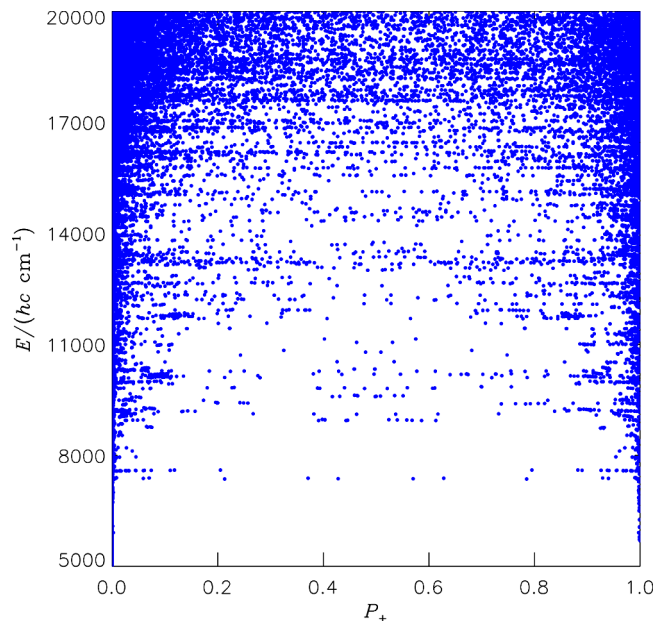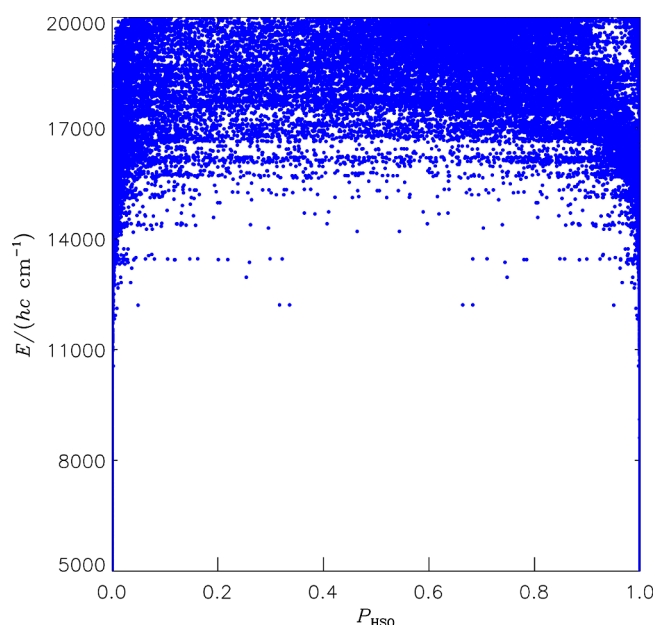

Figure 12. Term values in the interval 5000−20 000 cm^{-1} above the rovibronic ground state for all states of HSO/HOS with $J \leq 13/2$, plotted against P_+, the probability of finding the molecule in the $\tilde{A}\,^2A'$ state.

Figure 13. Term values in the interval 5000−20 000 cm^{-1} above the rovibronic ground state for all states of HSO/HOS with $J \leq 13/2$, plotted against P_{HSO}, the probability of finding the molecule on the HSO side of the isomerization barrier.

Figure 14. P_+, the probability of finding the HSO/HOS molecule in the Ã ^{2}A′ state, plotted against P_{HSO}, the probability of finding the molecule on the HSO side of the isomerization barrier, for all rovibronic states with term values less than 20 000 cm^{-1} above the rovibronic ground state and $J \leq 13/2$. Points corresponding to states with term values in the interval 0−14 000 cm^{-1} are plotted in blue. For states with term values in the ranges 14 000−16 000, 16 000−18 000, and 18 000−20 000 cm^{-1}, the corresponding colors are red, green, and black, respectively.

in particular in the low-energy parts of the figures. For Figure 12, this is a consequence of the fact that at energies so low that HSO/HOS isomerization is negligible, the Renner interaction takes place between states localized chiefly in the HOS minima of the X̃ ^{2}A″ and Ã ^{2}A′ electronic states. In this situation, the Renner mixing tends to give rise to pairs of mixed states, the two partner states having probabilities of P_+ and $1 - P_+$, respectively, of finding the molecule in the Ã ^{2}A′ state. An analogous tendency is seen for the low-energy states in Figure 13, but significant isomerization takes place chiefly at higher energies where the Renner interaction is also significant. Thus, there is no such thing as "pure" isomerization: an isomerizing rovibronic state belonging to, e.g., the X̃ ^{2}A″ electronic state will interact by the Renner effect with rovibronic states belonging to the Ã ^{2}A′ electronic state. Consequently, the states at higher energy in the P_{HSO} diagram of Figure 13 are less likely to separate into pairs of "mirror image" states in the manner seen in Figure 12.

Finally, in Figure 14 we investigate the correlation between the Renner interaction and the degree of isomerization for the HSO/HOS states whose energies and wave functions we have calculated. In this figure, we plot P_+ against P_{HSO} for states below 20 000 cm^{-1} with the plotted points color coded according to the term value of the state in question. The distribution of the points is a reflection of the MEP potential energy curves of Figure 3. Because the barrier to the H−S−O linear configuration is very high, a "pure" HSO state with $P_{HSO} \approx 1$ will have a very small Renner interaction; it will be either a pure X̃ ^{2}A″ state with $P_+ \approx 0$ or a pure Ã ^{2}A′ state with $P_+ \approx 1$.

This explains the clustering of points near (1.0, 0.0) and (1.0, 1.0) in Figure 14. A pure HOS state with $P_{HSO} \approx 0$ can have any amount of Renner interaction so there are points everywhere near the ordinate axis of the figure. The fact that to get an appreciable Renner interaction (that is, a value of P_+ neither near 0 nor near 1), it is necessary to have an appreciable probability of finding the molecule on the HOS side of the
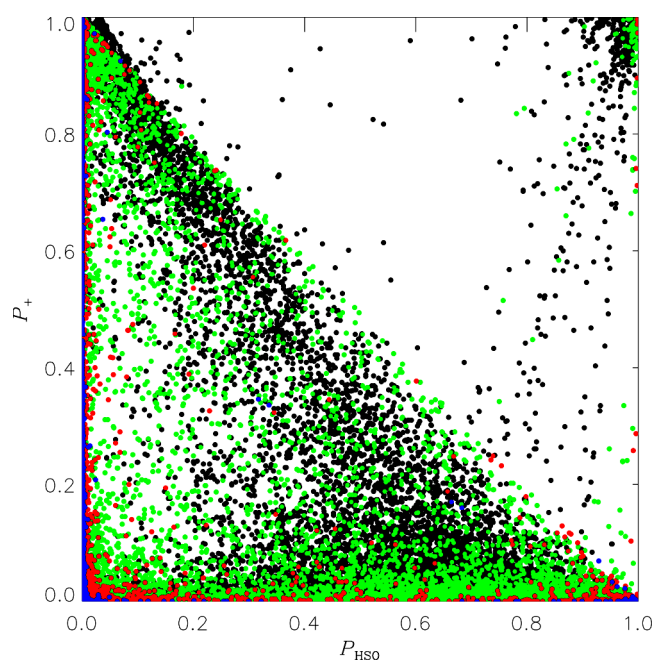
isomerization barrier (that is, a value of P_{HSO} significantly less than 1) causes the points to agglomerate in the area of Figure 14 defined by $P_+ + P_{HSO} \leq 1$. Because $P_{HOS} = 1 - P_{HSO}$, this inequality is equivalent to $P_+ \leq P_{HOS}$. This latter inequality quantifies our observation above that for a state to exhibit significant Renner interaction it must have a non-negligible value of P_{HOS}.

■ SUMMARY AND DISCUSSION

In the present work, we view the molecules HSO and HOS as one molecule HSO/HOS. Both in the electronic ground state X̃ ^{2}A″ and in the first excited electronic state Ã ^{2}A′, the HSO and HOS equilibrium structures correspond to different minima on a potential energy surface for HSO/HOS. We make here a theoretical calculation of the rovibronic energies for X̃- and Ã-state HSO/HOS, taking into account the HSO−HOS isomerization and the Renner interaction between the X̃ and Ã rovibronic states. The nuclear-motion calculations are carried out with the program DR[15−17] and are based on potential energy surfaces for the X̃ ^{2}A″ and Ã ^{2}A′ electronic states, calculated with the core-valence MR-SDCI+Q/[aug-cc-pCVQZ(S,O),aug-cc-pVQZ(H)] ab initio method.

As mentioned in the Introduction, at the present time theoretical simulations of rovibronic spectra for molecules of atmospheric and/or astrochemical interest are carried out almost exclusively within the Born−Oppenheimer approximation. That is, these theoretical calculations focus on one electronic state (normally the ground state) and its one potential energy surface only, and the influence from other electronic states (i.e., the breakdown of the Born−Oppenheimer approximation) is, at most, treated by perturbation

theory. Compared to the "ordinary" case of the Born–Oppenheimer approximation being essentially valid and the one potential energy surface considered having one minimum only, the theoretical description of the rotation and vibration in the electronic ground state $\tilde{X}\ ^2A''$ of HSO is subject to two complications. The first one is the presence of the Renner effect which causes the $\tilde{X}\ ^2A''$ state to be degenerate with the first excited state, $\tilde{A}\ ^2A'$, at linear geometries. As a consequence, the Born–Oppenheimer approximation breaks down and the $\tilde{X}$ $^2A''$ and $\tilde{A}\ ^2A'$ states must be treated together. The second complication is that in both the $\tilde{X}\ ^2A''$ and $\tilde{A}\ ^2A'$ electronic states, the potential energy minimum associated with the HSO equilibrium structure is separated from another minimum, corresponding to the equilibrium structure of the molecule HOS, by a barrier superable on the time scale of a typical spectroscopic experiment. In highly excited bending states the linear geometry S−O−H, associated with a doubly degenerate, $^2\Pi$ electronic state, becomes accessible to the molecule and the Renner interaction becomes important. Also, in these states there is tunneling between the two minima corresponding to HSO and HOS, respectively. The linear geometry H−S−O is also associated with a $^2\Pi$ electronic state but its electronic energy is so high that the resulting Renner interaction plays no significant role for the rovibronic states considered in the present work (Figure 3).

Our theoretical calculations show that as the energy increases, Renner interaction becomes significant for HSO/HOS around 7500 cm^{-1} above the vibronic ground state (which is localized in the $\tilde{X}$-state HSO minimum) whereas HSO/HOS isomerization starts at higher energies around 12 000 cm^{-1}. This is in keeping with the energetics of the $\tilde{X}\ ^2A''$ and $\tilde{A}\ ^2A'$ electronic states as presented in Figure 3. In Figures 7−11, we show how the combined effects of Renner interaction and HSO/HOS isomerization influence the vibrational motion of the molecule; these figures visualize the wave functions of a number of selected, exemplary rovibronic states of HSO/HOS in terms of probability density functions depending on the vibrational coordinates.

We illustrate in Figures 12 and 13 the connection between, on one hand, the energy of the rovibronic states considered and, on the other hand, their extent of Renner interaction and HSO/HOS isomerization, respectively. Finally, in Figure 14 we investigate the correlation between Renner interaction and isomerization. Owing to the fact that (Figure 3) the linear H−S−O geometry, with its associated Renner interaction, has an electronic energy so high that it is effectively inaccessible to the molecule in the rovibronic states that we consider here, there is no competition between Renner interaction and isomerization in HSO/HOS. For Renner interaction to take place, the molecule must have a significant probability of being found on the HOS side of the isomerization barrier. Consequently, the states suffering appreciable Renner interaction are either localized entirely in the HOS potential energy minimum or exhibit significant isomerization.

Together with NH$_2$[10] and HOO[18,19] that we have studied previously, HSO/HOS affords an example of a molecule whose electronic ground state suffers a breakdown of the Born–Oppenheimer approximation. In each of these three molecules, the Renner effect causes the potential energy surfaces for the electronic ground state and the first excited state to "stick together" at linear geometries. As a consequence, the two potential energy surfaces are, by necessity, energetically close and they must be treated together in calculations of the

rovibronic states with the interactions between them being described variationally. For HOO and HSO/HOS, the Renner effect is accompanied by isomerization and this further complicates the calculation of the rovibronic energies and wave functions. We hope to have demonstrated that also at moderate rovibronic energies, inteactions between electronic states can be sufficiently important that they must be treated variationally, and we believe that such treatments will make their way into theoretical simulations of rovibronic spectra for molecules of atmospheric and/or astrochemical interest in the foreseeable future.

■ ASSOCIATED CONTENT

ⓢ Supporting Information

List of the rovibronic energies calculated for HSO/HOS in the present work with tentative assignments. This material is available free of charge via the Internet at http://pubs.acs.org.

■ AUTHOR INFORMATION

Corresponding Author

*P. Jensen: e-mail, jensen@uni-wuppertal.de.

Present Address

§Institute of Applied Physics, Russian Academy of Science, Ulyanov Street 46, Nizhny Novgorod, Russia 603950.

Notes

The authors declare no competing financial interest.

■ ACKNOWLEDGMENTS

■ REFERENCES

(1) Tennyson, J. Accurate Variational Calculations for Line Lists to Model the Vibration-Rotation Spectra of Hot Astrophysical Atmospheres. *Wiley Interdiscip. Rev.: Comput. Mol. Sci.* **2012**, *2*, 698−715.

(2) Bunker, P. R.; Jensen, P. The Born-Oppenheimer Approximation. In *Computational Molecular Spectroscopy*; Jensen, P., Bunker, P. R., Eds.; Wiley: Chichester, U.K., 2000; see http://www.chem.uni-wuppertal.de/cms/.

(3) Buenker, R. J.; Liebermann, H.-P. Unpublished results.

(4) Santoro, F.; Petrongolo, C. Nonadiabatic Wave Packet Dynamics of NO$_2$ on the $\tilde{X}\ ^2A'/^2A'$ Conical Intersection. *J. Chem. Phys.* **1999**, *110*, 4419−4427.

(5) Sardar, S.; Mukherjee, S.; Kumar Paul, A.; Adhikari, S. Conical Intersections Between $\tilde{X}\ ^2A_1$ and $\tilde{A}\ ^2B_2$ Electronic States of NO$_2$. *Chem. Phys.* **2013**, *416*, 11−20.

(6) Renner, R. Zur Theorie der Wechselwirkung Zwischen Elektronen- und Kernbewegung bei Dreiatomigen, Stabförmigen Molekülen [in German]. *Z. Phys.* **1934**, *92*, 172−193.

(7) Jensen, P.; Osmann, G.; Bunker, P. R. The Renner Effect. In *Computational Molecular Spectroscopy*; Jensen, P., Bunker, P. R., Eds.; Wiley: Chichester, U.K., 2000.

(8) Brown, J. M. The Renner-Teller Effect: The Effective Hamiltonian Approach. In *Computational Molecular Spectroscopy*; Jensen, P., Bunker, P. R., Eds.; Wiley: Chichester, U.K., 2000.

(9) Tarroni, R.; Carter, S. Theoretical Calculation of Vibronic Levels of C$_2$H and C$_2$D to 10 000 cm^{-1}. *J. Chem. Phys.* **2003**, *119*, 12878/1−12.

(10) Jensen, P.; Odaka, T. E.; Kraemer, W. P.; Hirano, T.; Bunker, P. R. The Renner Effect in Triatomic Molecules with Application to CH$_2^+$, MgNC and NH$_2$. *Spectrochim. Acta Part A* **2002**, *58*, 763−794.

13463

dx.doi.org/10.1021/jp406940w | *J. Phys. Chem. A* 2013, 117, 13450−13464

(11) Jensen, P.; Brumm, M.; Kraemer, W. P.; Bunker, P. R. A Treatment of the Renner Effect Using the MORBID Hamiltonian. *J. Mol. Spectrosc.* **1995**, *171*, 31−57.

(12) Kolbuszewski, M.; Bunker, P. R.; Jensen, P.; Kraemer, W. P. An Ab Initio Calculation of the Rovibronic Energies of the BH_2 Molecule. *Mol. Phys.* **1996**, *88*, 105−124.

(13) Osmann, G.; Bunker, P. R.; Jensen, P.; Kraemer, W. P. A Theoretical Calculation of the Absorption Spectrum of CH_2^+. *Chem. Phys.* **1997**, *225*, 33−54.

(14) Kawakita, H.; Watanabe, J.-i.; Furusho, R.; Fuse, T.; Capria, M. T.; De Sanctis, M. C.; Cremonese, G. Spin Temperatures of Ammonia and Water Molecules in Comets. *Ap. J.* **2004**, *601*, 1152−1158.

(15) Odaka, T. E. The Double Renner Effect. *Ph.D. dissertation*, University of Wuppertal, Germany, and Ochanomizu University, Tokyo, Japan, 2003. See EPAPS Document No. E-JCPSA6-126-002708 for a pdf file with the Ph.D. thesis. This document can be reached via the EPAPS homepage http://www.aip.org/pubservs/epaps.html.

(16) Odaka, T. E.; Jensen, P.; Hirano, T. The Double Renner Effect: A Theoretical Study of the MgNC/MgCN Isomerization in the $\tilde{A}$ $^2\Pi$ Electronic State. *J. Mol. Struct.* **2006**, *795*, 14−41.

(17) Odaka, T. E.; Melnikov, V. V.; Jensen, P.; Hirano, T.; Lang, B.; Langer, P. Theoretical Study of the Double Renner Effect for $\tilde{A}$ $^2\Pi$ MgNC/MgCN: Higher Excited Rovibrational States. *J. Chem. Phys.* **2007**, *126*, 094301/1−9.

(18) Melnikov, V. V.; Odaka, T. E.; Jensen, P.; Hirano, T. The Double Renner Effect in the $\tilde{X}$ $^2A''$ and $\tilde{A}$ $^2A'$ Electronic States of HO_2. *J. Chem. Phys.* **2008**, *128*, 114316/1−10.

(19) Melnikov, V. V.; Jensen, P.; Hirano, T. Calculation of Rovibronic Intensities for Triatomic Molecules in Double-Renner-degenerate Electronic States: Application to the $\tilde{X}$ $^2A''$ and $\tilde{A}$ $^2A'$ Electronic States of HO_2. *J. Chem. Phys.* **2009**, *130*, 224105/1−9.

(20) Tennyson, J. Variational Calculations of Rotation-Vibration Spectra. In *Computational Molecular Spectroscopy*; Jensen, P., Bunker, P. R., Eds.; Wiley: Chichester, U.K., 2000.

(21) Friedl, R. R.; Brune, W. H.; Anderson, J. G. Kinetics of Mercapto (SH) with Nitrogen Dioxide, Ozone, Molecular Oxygen, and Hydrogen Peroxide. *J. Phys. Chem.* **1985**, *89*, 5505−5510.

(22) Lovejoy, E. R.; Wang, N. S.; Howard, C. J. Kinetic Studies of the Reactions of Mercaptooxy with Nitrogen Dioxide, Nitric Oxide, and Oxygen. *J. Phys. Chem.* **1987**, *91*, 5749−5755.

(23) Black, G. Reactions of HS with NO and NO_2 at 298 K. *J. Chem. Phys.* **1984**, *80*, 1103−1107.

(24) Wang, N. S.; Howard, C. J. Kinetics of the Reactions of Mercapto and Mercaptooxy with Ozone. *J. Phys. Chem.* **8794**, *1990*, 94−8787.

(25) Lee, Y.-Y.; Lee, Y.-P.; Wang, N. S. Kinetics of the Reaction of HSO with O_3 at Temperatures 273−423 K. *J. Chem. Phys.* **1994**, *100*, 387−392.

(26) Xantheas, S. S.; Dunning, T. H., Jr. Theoretical Estimate of the Enthalpy of Formation of Sulfhydryl Radical (HSO) and HSO-SOH Isomerization Energy. *J. Phys. Chem.* **1993**, *97*, 18−19.

(27) Esseffar, M.; Mó, O.; Yáñez, M. Is the Depletion of Ozone by HSO an Exothermic Process? *J. Chem. Phys.* **1994**, *101*, 2175−2179.

(28) Wilson, A. K.; Dunning, T. H., Jr. The HSO-HOS Isomers Revisited: The Effect of Tight d Functions. *J. Phys. Chem. A* **2004**, *108*, 3129−3133.

(29) Wang, N. X.; Wilson, A. K. Density Functional Theory and the Correlation Consistent Basis Sets: The Tight *d* Effect on HSO and HOS. *J. Phys. Chem. A* **2005**, *109*, 7187−7196.

(30) Li, B.-T.; Wei, Z.-Z.; Zhang, H.-X.; Sun, C.-c. Theoretical Studies on the Low-Lying Electronic States of the HSO Neutral Radical and Its Cation. *J. Phys. Chem. A* **2006**, *110*, 10643−10650.

(31) Schurath, U.; Weber, M.; Becker, K. H. Electronic Spectrum and Structure of the HSO Radical. *J. Chem. Phys.* **1977**, *67*, 110−119.

(32) Kakimoto, M.; Saito, S.; Hirota, E. Doppler-Limited Dye Laser Excitation Spectroscopy of the HSO Radical. *J. Mol. Spectrosc.* **1980**, *80*, 334−350.

(33) Satoh, M.; Ohashi, N.; Matsuoka, S.-i. Laser Excitation Spectrum of the $\tilde{A}$ $^2A'$ (004) ← $\tilde{X}$ $^2A''$ (000) Band of HSO Radical. *Bull. Chem. Soc. Jpn.* **1983**, *56*, 2545−2547.

(34) Ohashi, N.; Kakimoto, M.; Saito, S.; Hirota, E. Doppler-Limited Dye Laser Excitation Spectroscopy of the DSO Radical. *J. Mol. Spectrosc.* **1980**, *84*, 204−224.

(35) Ohashi, N.; Saito, S.; Suzuki, T.; Hirota, E. Dye Laser Excitation Spectroscopy of Two New Bands of the DSO Radical in 6100-Å Region. *J. Mol. Spectrosc.* **1988**, *127*, 481−496.

(36) Kawasaki, M.; Kasatani, K.; Tanahashi, S.; Sato, H.; Fujimura, Y. Fluorescence Lifetimes of Single Vibrational Levels in HSO ($\tilde{A}$ $^2A'$). *J. Chem. Phys.* **1983**, *78*, 7146−7152.

(37) Endo, Y.; Sato, H.; Hirota, E. Microwave Spectra of the HSO and DSO Radicals. *J. Chem. Phys.* **1981**, *75*, 4379−4384.

(38) Sears, T. J.; McKellar, A. R. W. The Laser Magnetic Resonance Spectrum of the v_3 Band of HSO at 10 μm. *Mol. Phys.* **1983**, *49*, 25−32.

(39) Yoshikawa, T.; Watanabe, A.; Sumiyoshi, Y.; Endo, Y. Laser Spectroscopy of the $\tilde{A}$ $^2A'$ − $\tilde{X}$ $^2A''$ System for the HSO Radical. *J. Mol. Spectrosc.* **2009**, *254*, 119−125.

(40) Langhoff, S. R.; Davidson, E. R. Configuration Interaction Calculations on the Nitrogen Molecule. *Int. J. Quantum Chem.* **1974**, *8*, 61−72.

(41) Woon, D. E.; Dunning, T. H., Jr. Gaussian Basis Sets for Use in Correlated Molecular Calculations. III. The Atoms Aluminum through Argon. *J. Chem. Phys.* **1993**, *98*, 1358−1371.

(42) Peterson, K. A.; Dunning, T. H., Jr. Accurate Correlation Consistent Basis Sets for Molecular Core-Valence Correlation Effects: The Second Row Atoms Al−Ar, and the First Row Atoms B−Ne Revisited. *J. Chem. Phys.* **2002**, *117*, 10548−10560.

(43) Dunning, T. H., Jr. Gaussian Basis Sets for Use in Correlated Molecular Calculations. I. The Atoms Boron through Neon and Hydrogen. *J. Chem. Phys.* **1989**, *90*, 1007−1023.

(44) Werner, H.-J.; Knowles, P. J.; Knizia, G.; Manby, F. R.; Schütz, M.; et al. *MOLPRO*, version 2010.1, a package of ab initio programs. See http://www.molpro.net.

(45) Bunker, P. R.; Jensen, P. *Molecular Symmetry and Spectroscopy*, 2nd ed.; NRC Research Press: Ottawa, 2006; see http://www.nrcresearchpress.com/doi/book/10.1139/9780660196282

(46) Numerov, B. Méthode Nouvelle de la Détermination des Orbites et le Calcul des Éphémérides en Tenant Compte des Perturbations [in French with Summary in Russian]. *Trudy Glavnoi Rossiiskoi Astrofizicheskoj Observatorii* **1923**, *2*, 188−259.

(47) Cooley, J. W. An Improved Eigenvalue Corrector Formula for Solving the Schrödinger Equation for Central Fields. *Math. Comput.* **1961**, *15*, 363−374.